Expert Systems With Applications 280 (2025) 127472

Contents lists available at ScienceDirect

Expert Systems With Applications

journal homepage: www.elsevier.com/locate/eswa

A computational model for multiobjective optimization of multipolar stimulation in cochlear implants: An enhanced focusing approach

Marcos Hernández-Gil [a], Ángel Ramos-de-Miguel [a,b], David Greiner [a,*], Domingo Benítez [a], Ángel Ramos-Macías [a,b], José M. Escobar [a]

[a] Institute of Intelligent Systems and Numerical Applications in Engineering (SIANI), Universidad de Las Palmas de Gran Canaria, Campus Universitario de Tafira Baja, Las Palmas de Gran Canaria, 35017, Las Palmas, Spain

[b] Department of Otolaryngology, Complejo Hospitalario Universitario Insular Materno Infantil de Gran Canaria, Las Palmas de Gran Canaria, 35002, Las Palmas, Spain

ARTICLE INFO

Keywords:
Cochlear implant
Multipolar stimulation
Finite element method
Evolutionary algorithms
Multiobjective optimization
Optimum design

ABSTRACT

Multipolar stimulation has been demonstrated to improve auditory perception in individuals with cochlear implants by generating more focused electric fields through simultaneous activation of multiple electrodes. In this study, we propose a novel approach to multipolar stimulation that aims to achieve the narrowest possible pattern of current densities at target neurons. Our goal is to find the optimal profile of currents delivered by the electrodes that maximizes the focusing for a specific power consumption, or alternatively, which minimizes the power for a given focusing. To this end, we have designed two objective functions which are optimized through multiobjective evolutionary algorithms. These objective functions are evaluated using a patient-specific finite element volume conduction model that replicates the cochlear geometry and electrical behavior of the implant. Experimental results demonstrate that this approach achieves tighter current density focusing compared to phased-array stimulation, albeit with higher power consumption. Additionally, it is possible to reach non-dominated solutions that simultaneously improve the focusing and power consumption of both monopolar and phased-array stimulation.

1. Introduction

One of the cochlear implant (CI) research interests consists in multipolar stimulation. In this context, we understand that a channel is the set of electrodes acting simultaneously and delivering the appropriate currents to stimulate a specific region of the auditory nerve. The aim of multipolar stimulation is to excite, for each channel, as narrow an area of the auditory nerve as possible. This type of stimulation produces more narrowly focused electric fields than monopolar stimulation (MP), in which only one electrode acts at each time instant.

1.1. State of the art

This section is organized around three key aspects of this work in relation to CI research: multipolar stimulation, patient-specific Finite Element Modeling (FEM), and Artificial Intelligence (AI) and computational intelligence techniques.

Firstly, works related to multipolar stimulation in CI are reviewed. Two types of strategies to produce intracochlear electric stimulation using multipolar focusing can be identified in the literature. They have been named *electrode focusing* and *neural focusing* (Saba, Elliott, & Wang, 2014). Electrode focusing tries to reduce electrode interaction from voltage spread associated with monopolar stimulation (van den Honert & Kelsall, 2007). Several forms of electrode focusing have been proposed and simulated using modeling studies: bipolar (BP), tripolar (TP), partial tripolar (pTP), phased-array (PA) (Cakmak, Pal, & Sahin, 2023; Randy K. Kalkman & Frijns, 2016). Multipolar stimuli produce localized potential peaks that are sharper than monopolar stimuli (Randy K. Kalkman & Frijns, 2016).

For the PA electrode focusing, the voltage pattern at the electrodes gives rise to a current pattern which is calculated by inverting the transimpedance matrix. For example, van den Honert and Kelsall (2007) consider that the optimum focusing around electrode p is achieved when all the potentials at the electrode site in the perilymph are 0 except that of the electrode p. In turn, neural focusing tries to achieve a sharper peak of the voltage distribution at the target neural

* Corresponding author.
E-mail addresses: marcosjavier.hernandez@ulpgc.es (M. Hernández-Gil), angel.ramos@ulpgc.es (Á. Ramos-de-Miguel), david.greiner@ulpgc.es (D. Greiner), domingo.benitez@ulpgc.es (D. Benítez), angelmanuel.ramos@ulpgc.es (Á. Ramos-Macías), josem.escobar@ulpgc.es (J.M. Escobar).

https://doi.org/10.1016/j.eswa.2025.127472
Received 30 October 2024; Received in revised form 20 February 2025; Accepted 27 March 2025
Available online 8 April 2025

pathway (Jolly, Spelman, & Clopton, 1996; Saba et al., 2014; Xu, Luo, & You, 2018).

Jolly et al. (1996) qualitatively compared the field distribution of monopoles, dipoles, and quadrupoles a distance from the plane of the sources. They calculated the potential predicted by a SPICE–based model of the first turn of the guinea pig inner ear at different points in the scala tympani (electrode focusing) and at the organ of Corti (neural focusing). This simulation demonstrates that a quadrupolar configuration focuses the potential and reduces the current spread better than the monopolar mode. However, the peak magnitude is considerably less than in the monopolar mode.

Saba et al. (2014) proposed a multipolar neural focusing strategy in which the voltage across neurons is obtained from the transimpedance matrix and currents at electrodes. They used a FEM-based analysis to show that focusing at the spiral ganglion cells significantly improved spatial selectivity compared with the strategy of just focusing at the electrode positions. However, one limitation of this strategy is that it would require significantly higher current levels than those needed in an electrode focusing strategy. So, a regularization coefficient was introduced into a novel cost function being minimized in order to improve current focusing and reduce current requirements. They showed that the effect of varying the regularization parameter on the voltage distribution along the spiral ganglion pathway consists in reducing the total current requirements. Nevertheless, the introduction of regularization may increase the number of activated neural regions.

A thin-film electrode array (TFEA) and partial tripolar (pTP) mode were combined by Xu et al. (2018) in the design stage to optimize the stimulation resolution (SR) of a CI at the auditory nerve fibers. A FEM model of the intracochlear electric potential, V_e, at the spiral ganglion neurons incorporating a TFEA and pTP mode was built and validated using previous experimental measurements. The SR was analyzed by using a defined stimulation factor V_s that quantify neural focusing. Two types of experiments were conducted, being the first analytical using a simplified geometry of the cochlea and representing the stimulating electrodes as point current sources. Additionally, a more elaborated FEM model was developed to analyze the electrode–cochlea system with the geometry of a TFEA and pTP mode. Using the analytical model, these authors calculated V_e along a line above the electrode surfaces where several spiral ganglion neurons would be located. A co-simulation method integrating the FEM model and genetic algorithm was employed to maximize V_s with an optimized parameter set including the electrode diameter, electrode interval, and compensation coefficient, which determines the current distribution in pTP mode. Results for V_e from the analytic and FEM models were compared with previous experimental results (Frijns, Dekker, & Briaire, 2011; Wu & Luo, 2016). Although some results are in accordance with previous findings, authors recognize that they used several simplifications such as a non-coiled shape of the cochlea or a non-real spatial distribution of the neurons that may sacrifice the accuracy of the simulation.

Secondly, works related to the development of patient-specific FEM models in CI are reviewed. They enable precise simulations fitted to individual anatomies and electrical properties. Advanced techniques, such as those proposed by Mangado et al. (2015), which employ statistical shape models, or by Kjer et al. (2018), which utilize statistical deformation models (SDM), enable the generation of precise geometries from medical imaging data, including CT scans. In addition to anatomical precision, some studies focus on adjusting the conductivity (or resistivity) parameters within FEM to better replicate electrical behavior. For instance, Nogueira, Schurzig, Büchner, Penninger, and Würfel (2016) developed a parametric model capable of predicting voltage distributions within the cochlea, incorporating patient-specific geometries and electrode placements to enhance accuracy. Liu (2023) present a method adjusting the model resistivities by deep learning.

Kalkman, Briaire, and Frijns (2015) examined various current focusing strategies that had been previously proposed using computational modeling studies of the implanted human cochlea. The investigation encompassed bipolar, partial tripolar and phased-array stimulation paradigms. A FEM model was used to incorporate realistic nerve fiber trajectories and tissue conductivities, which were derived from patient-specific intracochlear potentials. They showed that current focusing strategies require more power to attain adequate loudness levels compared to monopolar stimulation (Frijns et al., 2011; Randy K. Kalkman & Frijns, 2016). None of these focusing strategies employ an optimization procedure to calculate the configuration of input currents that increase spatial selectivity of neural excitation.

Thirdly, works related to the impact of AI and computational intelligence techniques in CI are reviewed. From that perspective recently Zhang et al. (2025) publish a survey about the increasing impact of AI in auditory prosthetics, covering from: speech enhancement and noise reduction, advanced signal processing techniques, to personalized rehabilitation strategies, and particularly highlighting the integration of AI with CIs. Another review related with AI and CI is the one presented in Essaid, Kheddar, Batel, Chowdhury, and Lakas (2024), focused mainly in covering advancements in CI-based automatic speech recognition and speech enhancement, among other related aspects. More specifically, from the perspective of optimum design with computational intelligence techniques in computational engineering and numerical simulation methods, Cassar, Titus, and Grill (2017) propose a single-objective genetic algorithm for designing optimal temporal patterns of neural stimulation, tested on two biophysically-based computational models of neural stimulation. The applied fitness function was an aggregate combination of measures related with energy requirements and other factors related with perceived pains or bradykinesia symptoms. In de Nobel, Kononova, Briaire, Frijns, and Bäck (2023) a surrogate model based on machine learning methods of an auditory nerve fiber is developed and optimized with a genetic algorithm (Wongsarnpigoon & Grill, 2010) to optimize the shape of the stimulus waveform in terms of energy efficiency. In Wongsarnpigoon and Grill (2010) a genetic algorithm was coupled to a computational model of extracellular stimulation of a mammalian myelinated axon, to determine the energy-optimal waveform shape for neural stimulation. Hussain, Grill, and Pelot (2024) propose a machine learning based surrogate fiber model that generates spatiotemporal responses to a wide variety of cuff-based electrical peripheral nerve stimulation protocols, for the design parameters of selective stimulation of pig and human vagus nerves. It was applied for optimization of neural fiber responses to electrical stimulation comparing a differential evolution optimization procedure with gradient descent; particularly optimization of the shape of charge-balanced waveforms to achieve spatially selective fiber activation was performed.

Considering the above references, none of them have tackled the optimization problem from a multi-objective perspective. Some of the previous methods tried to address only the optimization of spatially selective fibre activation (Hussain et al., 2024). Others addressed only energy efficiency aspects of the stimulus (de Nobel et al., 2023; Wongsarnpigoon & Grill, 2010). Some even combined energy efficiency aspects with other objectives (Cassar et al., 2017), but this was done in an aggregate form in a single objective. In the context of generating multipolar stimulation patterns in CIs, this work considers maximization of focusing and minimization of power consumption as conflicting objectives, whose optimization generates a set of non-dominated solutions that can be obtained by directly tackling a multi-objective optimization with stochastic global optimization algorithms (multi-objective evolutionary algorithms).

1.2. Motivation

As inferred from the cited research, multipolar stimulation has demonstrated considerable potential for enhancing auditory performance by generating more focused neural activation in comparison to conventional monopolar stimulation (Smith, Parkinson, & Long, 2013; Zhu, Tang, Zeng, Guan, & Ye, 2012). Nevertheless, despite its benefits in auditory discrimination, the counterpart of this technique is a higher

power consumption (Saba, 2012; Saba et al., 2014; Vellinga, Bruijn, Briaire, Kalkman, & Frijns, 2017; Zhu et al., 2012). The present study is motivated by the need to find a set of optimal profile of currents delivered by the electrodes that maximizes the focusing for a given power consumption, or alternatively, minimizes the power for a given focusing, in order to improve the performance of cochlear implants.

1.3. Contributions

In this article, we use an automated optimum design procedure based on computational intelligence techniques to achieve optimized multipolar stimulation patterns for cochlear implants. As far as we know, in the literature authors propose focusing strategies consisting on achieving a target voltage pattern either at the electrode sites or at the neurons. Here, we propose a novel approach to multipolar stimulation at the neuronal level based on current densities reaching target neurons, rather than potentials. The main contributions of the paper are:

1. Development of a patient-specific FEM model construction procedure utilizing a surrogate-based evolutionary algorithm.
2. Proposal of two objective functions, one for current density focusing on target neurons, and the other for power consumption.
3. Application of multiobjective evolutionary optimization techniques in which high-quality corner solutions are injected into the initial population, to find multipolar stimulation patterns in cochlear implants.

Experimental results show that the modeled current density can be focused more tightly than a phased-array stimulus, at the expense of higher power consumption. Moreover, more power-efficient stimulation is possible while improving the focusing of monopolar or phased-array stimuli.

1.4. Structure of the article

This paper presents a computational model for the multiobjective optimization of multipolar stimulation in cochlear implants. The construction of an electrically realistic model is performed by fitting the FEM model parameters so that the transimpedance matrix of the model approximate the clinical one. An introduction to the concepts of the transimpedance matrix is provided in Section 2. The fitting procedure of the FEM model is detailed in Section 3. In addition, in this section the objective functions for focusing and power consumption are defined. These functions are applied in a multiobjective optimization process to achieve optimal current profiles. The test cases and their respective results are presented in Section 4. The implications of the results and the potential impact of the proposed approach on cochlear implant technology are discussed in Sections 5 and 6, respectively.

2. Transimpedance matrix

The current input of a given electrode of a CI is a charge-balanced pulse train. The phase width and the interphase gap vary depending on the manufacturing company. For example, Cochlear (Cochlear® Ltd. Sydney, Australia) uses, for default, a biphasic stimulus with a phase width of 25 μs, an interphase gap width of 8 μs and a frame period of 1112 μs (see Fig. 1).

Let $\mathbf{i}(t) = \left(i_1(t), i_2(t), \ldots, i_E(t)\right)$ be the vector of the input current pulses from each electrode, where E is the number of electrodes. Let $\mathbf{I}(\omega)$ be the Fourier transform of $\mathbf{i}(t)$. Then, working in the frequency domain, we can write the potential at the electrodes as $\mathbf{V}(\omega) = \mathbf{Z}(\omega)\mathbf{I}(\omega)$, where $\mathbf{Z}(\omega) = \left(Z_{ij}(\omega)\right)$ is the transimpedance matrix and $\mathbf{I}(\omega)$ is the vector of the currents supplied by the electrodes. The entries of the transimpedance matrix $Z_{ij} = V_i/I_j$ are the relationships between the potential at the ith electrode and the input current at the jth

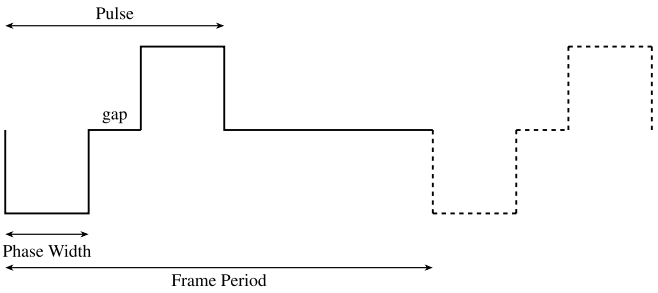

Fig. 1. Current input.

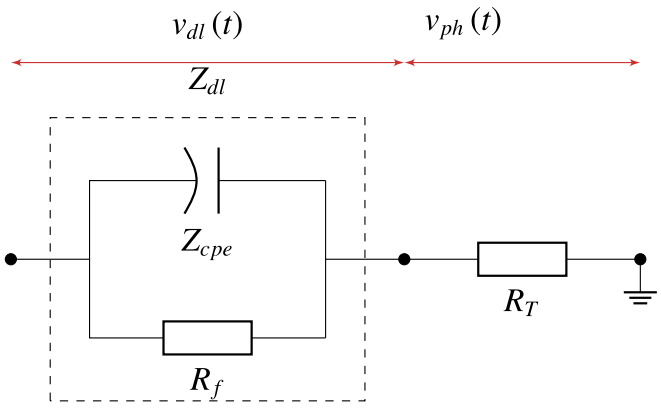

Fig. 2. Equivalent circuit of an active electrode.

electrode. Although we have not made it explicit, it is understood that all these quantities are frequency dependent. The terms of the diagonal, Z_{ii}, depend on the frequency due to the double layer interface formed between the electrolyte and the electrode, and therefore, they are complex. Several equivalent circuits have been proposed to model these impedances (see, for example, Aebischer, Meyer, Caversaccio, & Wimmer, 2021; Cantrell, Inayat, Taflove, Ruoff, & Troy, 2007; Franks, Schenker, Schmutz, & Hierlemann, 2005; McAdams & Jossinet, 1992; Mesnildrey, Venail, Carlyon, & Macherey, 2020; Richardot & McAdams, 2002). In essence, all of them are variations of a circuit formed by the sum of two impedances $Z_{DL} + R_T$.

The first impedance, Z_{DL} represents the electrolyte-electrode interface, approximated by the parallel combination of a nonfaradaic pseudocapacitance

$$Z_{cpe} = K(j\omega)^{-\beta} \tag{1}$$

where β and K are constants, and a faradaic transfer resistance R_f derived from the Butler–Volmer equation. Values of β and K and Rf can be found in McAdams and Jossinet (1992), Richardot and McAdams (2002), Cantrell et al. (2007) and Mesnildrey, Macherey, Herzog, and Venail (2019). For example, the average value for 8 patients of $Y_0 = K^{-1}$ given in Mesnildrey et al. (2019), for an electrode with a surface of $0.2\times0.4\text{mm}^2$, is $481\times10^{-9}\,\Omega^{-1}\text{s}^{\beta}$, and $\beta = 0.64$. The resulting impedance is $Z_{cpe} = 2.079\times10^{6}(j\omega)^{-0.64}\Omega$. For this electrode the value of $R_f = 4.9\times10^{7}\,\Omega$, is extremely high and can be removed from the equivalent circuit, so $Z_{Dl} \approx Z_{cpe}$.

The second impedance, R_T, is purely resistive and represents the sum of the resistances due to the electrolyte, tissues and conductors.

The off-diagonal terms of $\mathbf{Z}$ represent the potentials reached by one electrode produced by the current arising from another electrode and they are purely resistive elements (van den Honert & Kelsall, 2007). All of the above suggests that we write the transimpedance matrix as the sum of two matrices,

$$\mathbf{Z}(\omega) = \mathbf{D}(\omega) + \mathbf{Z}_c \tag{2}$$

The first matrix $\mathbf{D}(\omega)$, is diagonal and introduces the complex impedance, Z_{DL}, due to the double layer interface. The values of Z_{DL} vary according to the electrode and patient under consideration (Mesnildrey et al., 2020). The diagonal terms of $\mathbf{Z}_c$ represent the resistance R_T of the equivalent circuit of the Fig. 2. The off-diagonal terms of $\mathbf{Z}_c$ coincide with those of $\mathbf{Z}$. For all this, the matrix $\mathbf{Z}_c$ is purely resistive (real).

The potential at the electrodes due to the current vector $\mathbf{I}(\omega)$ is given by

$$\mathbf{V}(\omega) = \mathbf{D}(\omega)\mathbf{I}(\omega) + \mathbf{Z}_c\mathbf{I}(\omega) \tag{3}$$

The second sumand in (3) is the vector of the potentials at the electrode sites in the perilymph $\mathbf{V}_{ph}(\omega) = \mathbf{Z}_c\mathbf{I}(\omega)$. The usual clinical telemetry only allows the measurement of the off-diagonal inputs of $\mathbf{Z}_c$, since they coincide with those of the transimpedance matrix $\mathbf{Z}(\omega)$. The diagonal terms of $\mathbf{Z}_c$ must be estimated by approximate methods through the off-diagonal entries of $\mathbf{Z}_c$.

Note that we are working in the frequency domain, so, to calculate the potentials and currents in the time domain, we have to perform the inverse Fourier transform. Thus, if $\mathbf{i}(t)$ is the input current vector at the electrodes, the corresponding potential vector, $\mathbf{v}(t)$, is given by

$$\begin{aligned}\mathbf{v}(t) =& \mathcal{F}^{-1}(\mathbf{Z}(\omega)\mathbf{I}(\omega)) = \\ & \mathcal{F}^{-1}(\mathbf{D}(\omega)\mathbf{I}(\omega)) + \mathbf{Z}_c\mathcal{F}^{-1}(\mathbf{I}(\omega)) = \\ & \mathcal{F}^{-1}(\mathbf{D}(\omega)\mathbf{I}(\omega)) + \mathbf{Z}_c\mathbf{i}(t) = \\ & \mathbf{v}_{dl}(t) + \mathbf{v}_{ph}(t)\end{aligned} \tag{4}$$

where $\mathbf{v}_{dl}(t) = \mathcal{F}^{-1}(\mathbf{D}(\omega)\mathbf{I}(\omega))$ is the voltage drop in time domain associated to the electrode electrolyte double layer, which is the responsible of the distortion suffered by the potential with respect to the input $\mathbf{i}(t)$. The term $\mathbf{v}_{ph}(t) = \mathbf{Z}_c\mathbf{i}(t)$ is the potential in the perilymph at the electrode positions. These are the potentials that are enforced to be all null, except the one corresponding to the target electrode, in the phased array (PA) stimulation proposed in van den Honert and Kelsall (2007). The potential $\mathbf{v}_{ph}(t)$ and the intensity $\mathbf{i}(t)$ are in phase, since the matrix $\mathbf{Z}_c$ is purely resistive.

3. Optimum multipolar stimulation

This section covers the description of the optimum multipolar stimulation procedure. First, Section 3.1 deals with threshold current density. In Section 3.2 it is described how an electrically realistic model is constructed. In Section 3.3 the FEM conductive model is explained. Then in Section 3.4, the objective functions for focusing and power consumption optimization are introduced. Finally, the multiobjective optimum design method is exposed in Section 3.5.

3.1. Threshold current density

When an electrode injects a current, the neurons located in its surroundings are excited. There are numerous works (see, for example, the review article Tehovnik, Tolias, Sultan, Slocum, and Logothetis (2006)) that study the relationship between the injected current and the extension of the region of neurons triggered by this current. They show that the threshold input current amplitude, I_{th}, required to activate neurons located at distance r from the stimulating electrode tip is given by

$$I_{th} = K_e r^2 \tag{5}$$

The values of the excitability constant K_e depend, among other things, on the type of neuron and the input waveform. This constant has been measured empirically by many authors using different types of neurons from many animals (Tehovnik et al., 2006). An electrode can be considered as a point source of current at sufficiently large distances (on the order of several times the size of the electrode). The current density produced by a point source is given by $J = I/4\pi r^2$. Introducing this expression into (5), it is deduced that the threshold current density J_{th} is

$$J_{th} = \frac{K_e}{4\pi} \tag{6}$$

This result shows that an action potential is elicited if the most excitable areas of a neuron, which for myelinated neurons are the nodes of Ranvier, reach a current density greater than or equal to J_{th}.

The existence of a threshold current density is consistent with computational models based on the Hodgkin–Huxley (HH) equations (Hodgkin & Huxley, 1952). In these models, the trigger of the action potential is the external current density passing through the neurons. Its threshold value for producing an action potential depends on the particular parameters of the HH model and the waveform of stimulus. Thus, taking the parameters given in Dokos (2017) and an input current density with the waveform of Fig. 1, it is possible to verify through a numerical simulation that the threshold amplitude that gives rise to an action potential is $J_{th} = 2.8\,\mathrm{A\,m^{-2}}$. As will be seen in Section 3.4.1, our computational model predicts that, in monopolar stimulation, this current density is achieved in the auditory nerve region closest to the active electrode when the input current amplitude is around 0.04 mA. Henkin, Kaplan-Neeman, Muchnik, Kronenberg, and Hildesheimer (2003)'s work evaluates the threshold levels of stimulation (T levels) and their variation over time. The observed values range from 60 to 80 current levels, equivalent to 0.05 mA to 0.07 mA for Cochlear devices. These values represent the minimum current required for patients to start auditory sensation, which implies the stimulation of a group of neurons. In our simulation case, it is essential to note that we are determining the threshold for a single neuron.

The number of neurons that exceeds J_{th} depends on the amplitude and pattern of the input currents $\mathbf{i}(t)$. To determine whether one current density profile is more focusing than another, we will normalize these profiles. To this end, we will choose the amplitude of $\mathbf{i}(t)$ that produces a maximum current density in the target region, J_{max}, of value one, that is, $J_{max} = 1\,\mathrm{A\,m^{-2}}$. This topic will be discussed in detail in Section 3.4.

The above results suggest that we focus our efforts on achieving an input current pattern that results in a normalized current density distribution that is centered on the target area of the auditory nerve and that is as narrow as possible. This strategy differs from those proposed in previous works, in which they focused their efforts on achieving focused multipolar stimulation by imposing a certain pattern of potentials on electrodes or neurons.

3.2. Construction of an electrically realistic model

The first task we must perform is to build a FEM model that represents, as faithfully as possible, the potentials and current densities that appear in the cochlea when a certain channel is activated. Our model is not intended to simulate the double layer phenomenon, associated with the $\mathbf{D}$ matrix, but to characterize the electrical behavior that allows us to calculate the potential and currents inside the cochlea, from which the conducting part of the transimpedance matrix, $\mathbf{Z}_c$, is derived. To this end, we will implement a volume conduction model (see e.g., Callejón-Leblic, Lazo-Maestre, Fratter, Ropero-Romero, Sánchez-Gómez et al., 2024; Hanekom & Hanekom, 2016; Malherbe, Hanekom, & Hanekom, 2015a, 2015b; de Miguel et al., 2022; Potrusil et al., 2020).

To accurately model the currents produced by the CI, we should have precise knowledge of the geometry and electrical properties of all the tissues that make up the cochlea and the rest of the head. This knowledge is practically impossible due to the complexity of these structures and the variability that exists between patients. To bypass this problem we have opted to construct a simplified conductive model in which the cochlea is included in a sphere containing a medium whose conductivity, σ_{ext}, must be adjusted so that the matrix of the model, $\mathbf{Z}_{c,m}$, and that of the patient under consideration, $\mathbf{Z}_{c,p}$, are as similar as possible.

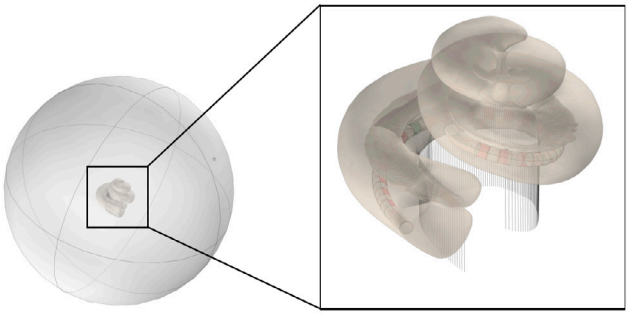

Fig. 3. Surrounding sphere of the FEM model and a zoom of the implanted cochlea with perimodiolar inserted electrode array.

The model consists, in addition to σ_{ext}, of two additional parameters that must be adjusted to match both matrices. One of these parameters is the conductivity of a layer covering the outer surface of the cochlea, σ_{bone}, which mimics the high-density bone covering the real cochlea. The construction of this layer involves a great difficulty from the geometrical and mesh generation point of view. Since the layer is thin and its conductivity is low compared to the surrounding tissue, it is possible to bypass the construction of the layer by imposing a contact impedance condition that emulates its effect.

The other parameter is the conductivity of the perilymph, σ_{per}, whose values may vary between $[1.0, 2.0]\,\mathrm{S\,m^{-1}}$, depending on the reference consulted Aebischer et al. (2021). To summarize, we have three fitting conductivities, $\boldsymbol{\sigma} = (\sigma_{ext}, \sigma_{bone}, \sigma_{per})$, that are the variables of an objective function that measures the difference between $\mathbf{Z}_{c,m}$ and $\mathbf{Z}_{c,p}$. The variation range of σ_{ext} is $[0.2, 1.42]\,\mathrm{S\,m^{-1}}$ and that of σ_{bone} is $[0.01, 0.1]\,\mathrm{S\,m^{-1}}$. The optimum conductivities, $\boldsymbol{\sigma}_{opt}$, are those resulting from the minimization of this objective function. The minimization is carried out using an optimization procedure that will be described in the next Section 3.2.1.

The computational model of the cochlea includes an electrode array of 22 electrodes embedded in a silicone carrier similar to the Cochlear Nucleus™ Profile CI512 electrode array. The conductivity of the silicone of this carrier is $\sigma_{silicone} = 1 \times 10^{-14}\,\mathrm{S\,m^{-1}}$. The length and the radius of the array are 14 mm and 0.2 mm, respectively. The dimensions of the electrodes are $0.7 \times 0.3\ \mathrm{mm^2}$ and the inter-electrode distance is 0.7 mm.

Since we are interested in current densities in auditory nerve fibers, we have to include in our model an approximate representation of these fibers. This is achieved by means of a set of virtual neurons (VNs) which are just curves that imitate the trajectories of real neurons and are used to determine the values of current densities in realistic positions. The density of real neurons in the auditory nerve is much higher than the density of VNs in our computational model, so each VN represents a large number of real neurons.

3.2.1. Optimization procedure to determine the optimum conductivities

Our objective is to calculate the conductivities $\boldsymbol{\sigma} = (\sigma_{ext}, \sigma_{bone}, \sigma_{per})$ that minimize the difference between the impedance matrices of the patient, $\mathbf{Z}_{c,p}$, and of the model, $\mathbf{Z}_{c,m}$. If we denote $\boldsymbol{\Delta}_c = \mathbf{Z}_{c,p} - \mathbf{Z}_{c,m}$ as the difference of both matrices, the selected objective function is the Frobenius norm of $\boldsymbol{\Delta}_c = (\delta_{ij})$

$$R = \|\boldsymbol{\Delta}_c\|_F = \sqrt{\sum_{i=1}^{E}\sum_{j=1}^{E} |\delta_{ij}|^2} \tag{7}$$

where E is the number of electrodes of the CI. Since clinical measurements do not allow us to determine the diagonal terms of $\mathbf{Z}_{c,p}$ and thus calculate δ_{ii}, we will consider $\delta_{ii} = 0$ in the calculations of $\|\boldsymbol{\Delta}_c\|_F$.

Every evaluation of the objective function involves the execution of a FEM simulation of the model (as described in Section 3.2), to calculate $\mathbf{Z}_{c,m}$. Therefore, an evolutionary algorithm as global optimizer with the only requirement of being able to evaluate the objective function (e.g. without any derivability condition), will be used. In order to speed-up the optimization of the evolutionary algorithm, which requires a high number of objective function evaluations, the process will be supported with the construction of a surrogate model with much lower evaluation cost (without the need to evaluate the FEM simulation); that is, a surrogate assisted evolutionary optimization will be afforded. The steps of the procedure to attain the optimum conductivities, $\boldsymbol{\sigma}_{opt}$, in order to achieve a computational cochlear model approximately fitted to patient transimpedance matrix data are detailed as follows (see Fig. 4).

1. As initial sampling (Design of Experiments), a Latin Hypercube Sampling (Viana, 2015) with full factorial approach is performed to propose the set of conductivities $\{\boldsymbol{\sigma}^i\}_{i=1}^N$, where N is the number of samples.
2. The set $\{\boldsymbol{\sigma}^i\}_{i=1}^N$ is introduced into our FEM model to obtain the set of the impedance matrices $\{\mathbf{Z}_{c,m}^i\}_{i=1}^N$.
3. These FEM matrices are compared to the patient's impedance matrix, $\mathbf{Z}_{c,p}$, and the objective function defined in Eq. (7) is evaluated. In this way, a set $\{R^i\}_{i=1}^N$ is obtained which is used to train the *Kriging* surrogate model.
4. Several Kriging models were tested: four types of correlation functions were taken into account: exponential, squared exponential, matern 5/2, and matern 3/2; with constant, linear or quadratic model for the deterministic term, as explained in Bouhlel, Hwang, Bartoli, Lafage, Morlier et al. (2019). The Kriging model with best test set accuracy is chosen after a split of the whole sampling data consisting in training set and test set.
5. Once the initial surrogate model was built, a surrogate assisted evolutionary optimization was performed (Ruan, Li, Derbel, & Liefooghe, 2020) using differential evolution (Price, 2013) as global optimizer and the abovementioned Kriging model as surrogate. Several independent executions were run, and the best solution $\bar{\boldsymbol{\sigma}}$ was chosen to proceed with the next step.
6. A local search near the optimum $\bar{\boldsymbol{\sigma}}$ was performed. For this purpose, we construct a reduced set of conductivities $\{\bar{\boldsymbol{\sigma}}^j\}_{j=1}^M$ centered on $\bar{\boldsymbol{\sigma}}$, where M is the number of samples.
7. The set $\{\bar{\boldsymbol{\sigma}}^j\}_{j=1}^M$ is introduced into our FEM model to obtain the set of the impedance matrices $\{\bar{\mathbf{Z}}_{c,m}^j\}_{j=1}^M$.
8. Comparing these matrices with the clinical impedance matrix, $\mathbf{Z}_{c,p}$, we evaluate the objective function (7) to obtain $\{R^j\}_{j=1}^M$. The optimum conductivity, $\boldsymbol{\sigma}_{opt}$, is the one that minimizes $\{R^i\}_{i=1}^N \cup \{R^j\}_{j=1}^M$ and the $\mathbf{Z}_{c,m}^{opt}$ matrix is the $\mathbf{Z}_{c,m}$ matrix calculated with the conductivities $\boldsymbol{\sigma}_{opt}$.

3.3. Conductive model

The conductive model is governed by the Laplace equation

$$\nabla \cdot \sigma \nabla \phi = 0 \quad \text{in} \quad \Omega \tag{8}$$

where ϕ is the electric potential and σ is the conductivity. The domain Ω is formed by the cochlea and the surrounding sphere, see Fig. 3. The current density is given by $\mathbf{J} = \sigma_n \mathbf{E}$, with $\mathbf{E} = -\nabla\phi$, where σ_n is the conductivity of the nth tissue or fluid, which is considered to be purely resistive (real). The potential and currents involved in the model can be considered as the amplitudes of the corresponding time signals.

3.3.1. Boundary conditions

Active and disconnected electrodes

An active electrode is characterized by delivering a certain current I_0, while a disconnected electrode is one through which no current flows, it is a floating conductor. Thus, if S_e be the surface of an

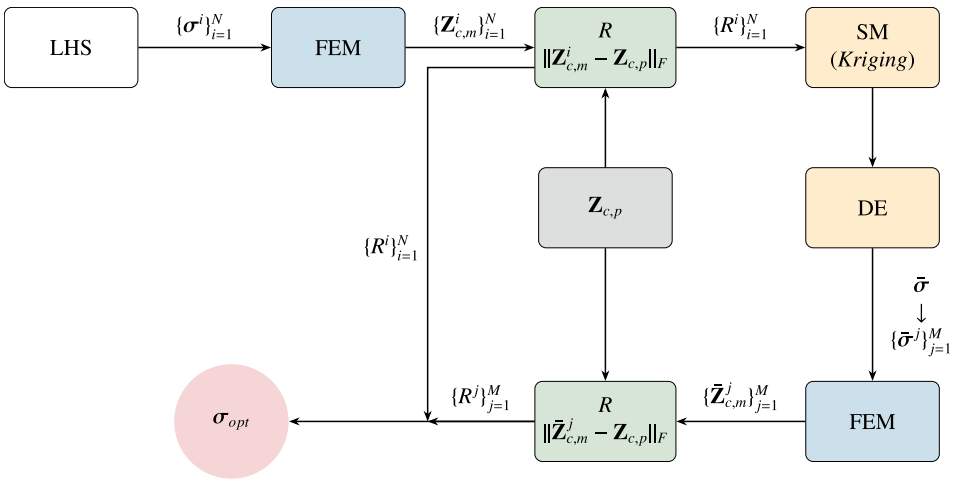

Fig. 4. Flowchart of the process of optimizing the conductivities of the FEM model.

active or disconnected electrode delivering a current I_0 ($I_0 = 0$ if it is disconnected), it must satisfy the condition

$$-\sigma \oint_{S_e} \mathbf{n} \cdot \nabla\phi \, da. = I_0 \tag{9}$$

where $\mathbf{n}$ is the outgoing unitary normal vector to S_e and σ the conductivity of the surrounding media. Note that part of the electrodes are embedded in silicone, so $\sigma \approx 0$ in this part of S_e, which means that almost no current is delivered through the silicone.

The constraint (9) is not properly a boundary condition, since it cannot be imposed directly in the differential equation. However, it can be easily transformed into a true-type boundary condition. As an example, if we have only a single electrode and it is active, we can impose the condition (9) as follows. Let ϕ_1 be the solution to Eq. (8) with S_e at potential 1 V, the linearity of the Laplace equation requires that the solution of our problem must be $\phi = \lambda\phi_1$, with λ an appropriate constant. Note that this is because in both cases S_e is a equipotential. The value of λ is calculated by imposing the condition (9).

The procedure to impose condition (9) is similar when there is more than one electrode and at least one of them is active, but in that case we need as many linearly independent solutions as electrodes. An example of how to impose condition (9) in the case of having one active and one floating electrode is shown in de Miguel et al. (2022).

Reference electrode and surrounding sphere

The reference electrode is taken as ground $\phi = 0$. The boundary of the domain, $\partial\Omega$, is the surrounding sphere. It is considered to be an isolating surface $\mathbf{J} \cdot \mathbf{n} = 0$, so that the boundary condition is

$$\frac{\partial\phi}{\partial\mathbf{n}} = 0 \quad \text{in} \quad \partial\Omega \tag{10}$$

3.4. Objective functions for focusing and power consumption optimization

In this section we will define the objective functions used to maximize the focusing and minimize the power consumed by the CI. These are the two objective functions of a multiobjective optimization process that aims to determine the set of non-dominated solutions that provide the profile of currents feeding the electrodes to achieve the maximum possible focusing for a given power consumption, or alternatively seen, the minimum power for a given focusing.

3.4.1. Objective function for focusing

Multipolar stimulation aims to minimize the current dispersion that occurs when a particular channel is activated. Each channel should concentrate the current in an area of the auditory nerve as narrow as possible. Recall that a channel is the set of currents that the electrodes must deliver to excite a specific area of the auditory nerve. Thus, let us consider that channel k is responsible to excite the neural region close to electrode k. For each channel k, we look for the pattern of currents supplied by the electrodes that maximize the current densities reaching the VNs near electrode k and minimize the current densities reaching the other VNs. Our goal is to design a suitable objective function for this task.

Let $\phi_i(\mathbf{x})$, $i = 1, \ldots, E$, be the potential in any point $\mathbf{x} \in \Omega$ due to the current source at electrode i delivering an intensity $I_0 = 1$ A, where E is the number of electrodes of the CI. The linearity of Eq. (8) allows any solution to be written as a linear combination of these solutions

$$\phi(\mathbf{x}) = \sum_{i=1}^{E} \alpha_i' \phi_i(\mathbf{x}) \tag{11}$$

Consequently, we can write the current density as

$$\mathbf{J}(\mathbf{x}) = \sum_{i=1}^{E} \alpha_i' \mathbf{J}_i(\mathbf{x}) \tag{12}$$

where $\mathbf{J}_i = -\sigma\nabla\phi_i$. Note that the vector of coefficients (dimensionless) $\boldsymbol{\alpha}' = (\alpha_i')$ are numerically equal to the vector of currents delivered by the electrodes.

To obtain a normalized profile of current densities in the modiolar region we must define appropriate coefficients α_i, so that the maximum current density over the VNs is unity. In this way, we can compare the focusing of different input current profiles.

Let us consider that, for a given set of coefficients $\boldsymbol{\alpha}' = (\alpha_i')$, J_{max}^n is the maximum of $\|\mathbf{J}\|$ at the nth VN, that is,

$$J_{max}^n = \max_{\mathbf{x} \in \mathrm{VN}_n} \|\mathbf{J}(\mathbf{x})\| \tag{13}$$

Let $J_{max} = \max_{1 \le n \le N_n} J_{max}^n$ be the maximum current density reached by any of the N_n VNs. The current density norm along the selected neurons for a monopolar stimulation of electrode 12 with 1 mA is shown on the left side of Fig. 5, where J_{max}^n and J_{max} are represented by red dots and a cross, respectively. On the right side of Fig. 5, the values of J_{max}^n for all neurons are shown. The selected neurons of the left graph are indicated by red markers. In this case, $J_{max} = 67\,\mathrm{mA\,m^{-2}}$ for an input current of 1 mA, so to reach the value of $J_{th} = 2.8\,\mathrm{A\,m^{-2}}$, which gives rise to an action potential in the HH computational model, the input current must be 0.04 mA, as commented in Section 3.1.

We define the vector of normalized current coefficients as

$$\boldsymbol{\alpha} = \frac{\boldsymbol{\alpha}'}{N(J_{max})} \tag{14}$$

where $N(J_{max})$ is the numeric value of J_{max}, that is, $N(J_{max}) = J_{max}\,\mathrm{A\,m^{-2}}/1\,\mathrm{A\,m^{-2}}$ (dimensionless). The normalized coefficients $\boldsymbol{\alpha}$ produce a maximum current density of 1 $\mathrm{A/m^2}$ in at least one of the N_n VNs.

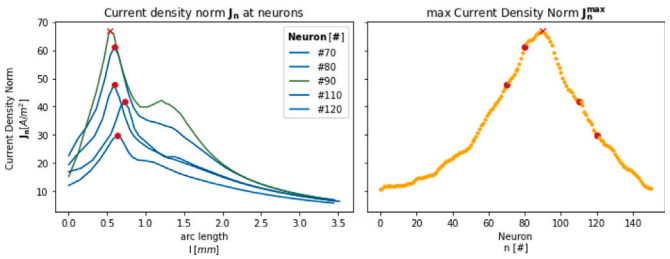

Fig. 5. The graph on the left displays the norm of the current density along the selected neurons for monopolar stimulation of electrode 12 with 1 mA. The red dots and cross indicate the values of J^n_{max} and J_{max}, respectively. The graph on the right shows the maximum values of the current density for all neurons, with the red markers indicating the selected neurons.

From now on, we will write $\mathbf{j}(\mathbf{x})$ to refer to the normalized current density, that is,

$$\mathbf{j}(\mathbf{x}) = \sum_{i=1}^{E} \alpha_i \mathbf{J}_i(\mathbf{x}) \tag{15}$$

The maximum of $\|\mathbf{j}(\mathbf{x})\|$ at the nth VN is

$$j^n_{max} = \max_{\mathbf{x}\in \mathrm{VN}_n} \|\mathbf{j}(\mathbf{x})\| \tag{16}$$

and verify $0 \le j^n_{max} \le 1$.

The goal is to find the current coefficients $\boldsymbol{\alpha}$ such that $j^n_{max}(\boldsymbol{\alpha})$ be 1 at the VNs around the electrode k (the target region) and 0 at the other VNs. More precisely, if $\mathrm{VN}(k) = \{k_1, k_2 \dots, k_M\}$ is the set of indexes of the M VNs closer to electrode k than to the other electrodes, the objective function is

$$F(\boldsymbol{\alpha}) = w \sum_{m\in \mathrm{VN}(k)} \left(1 - j^m_{max}(\boldsymbol{\alpha})\right)^2 + \sum_{n\notin \mathrm{VN}(k)} \left(j^n_{max}(\boldsymbol{\alpha})\right)^2 \tag{17}$$

where w is a constant parameter whose role is to balance the weight of the two summands of the objective function. The values of this function are included in the interval $[0, F_{max}]$, being $F_{max} = N_n - M + wM$, N_n the total number of VNs and M is the number of neurons belonging to $\mathrm{VN}(k)$.

Note that the higher the values of $F(\boldsymbol{\alpha})$, the lower the focusing will be. Thus, this function gives us an idea of dispersion rather than focusing. However, we can construct an objective function for focusing as

$$F_c(\boldsymbol{\alpha}) = F_{max} - F(\boldsymbol{\alpha}) \tag{18}$$

so that the maximization of $F_c(\boldsymbol{\alpha})$ implies a maximization of the focusing. The values of this function are included in the interval $[0, Fmax]$. Therefore, we can pose the problem in two equivalent ways, either minimizing the dispersion $F(\boldsymbol{\alpha})$ or maximizing the focusing $F_c(\boldsymbol{\alpha})$. This optimization process must be performed for each channel. Obviously, each channel will have its own optimum vector of coefficients $\boldsymbol{\alpha}$.

3.4.2. Objective function for power

Our interest is now focused on calculating, for each channel, the power associated with its current pattern. We want to know whether a given current configuration consumes more or less power than another. In particular, we want to compare the consumption of a given configuration with those corresponding to monopolar and multipolar stimulation. The power consumption depends on the waveform and the amplitude of the input signal. To set a criterion for power comparison, we will assume that two different configurations corresponding to the same channel must reach the same maximum current density. This requirement is achieved by working with the normalized coefficients $\boldsymbol{\alpha}$.

Let $I_{unit}(\omega) = \mathcal{F}\left(i_{unit}(t)\right)$ be the current, in the frequency domain, corresponding to an input pulse $i_{unit}(t)$ of unit amplitude (1 A peak value) and duration T, similar to the one shown in Fig. 1.

Then, the currents delivered by the electrodes for a given set of coefficients $\boldsymbol{\alpha} = (\alpha_i)$ are $\mathbf{i}(t) = i_{unit}(t)\boldsymbol{\alpha}$ in the time domain and $\mathbf{I}(\omega) = I_{unit}(\omega)\boldsymbol{\alpha}$ in the frequency domain.

The instantaneous power consumed by the CI due to the currents flowing through the electrolytes and tissues of the inner ear and head is $\mathbf{i}(t)^{\mathrm{T}}\mathbf{v}_{ph}(t) = \mathbf{i}^{\mathrm{T}}(t)\mathbf{Z}_c\mathbf{i}(t)$, where $\mathbf{Z}_c$ is the transimpedance matrix computed by FEM ($\mathbf{Z}_c \equiv \mathbf{Z}_{c,m}$ in this context). Therefore, the average power of the pulse is

$$\begin{aligned} P_{avg} &= \frac{1}{T}\int_0^T \mathbf{i}^{\mathrm{T}}(t)\mathbf{Z}_c\mathbf{i}(t)\,dt = \\ &= \boldsymbol{\alpha}^{\mathrm{T}}\mathbf{Z}_c\boldsymbol{\alpha}\left(\frac{1}{T}\int_0^T i^2_{unit}(t)\,dt\right) \end{aligned} \tag{19}$$

The last integral term of Eq. (19) is a constant that only depends on the specific characteristic of the input pulse. It can be calculated through $I_{unit}(\omega)$ by applying the Plancherel's theorem

$$K_{input} = \frac{1}{T}\int_0^T i^2_{unit}(t)\,dt = \frac{1}{2\pi T}\int_{-\infty}^{\infty} |I_{unit}(\omega)|^2 d\omega \tag{20}$$

Thus, the average power can be written as

$$P_{avg} = K_{input}\boldsymbol{\alpha}^{\mathrm{T}}\mathbf{Z}_c\boldsymbol{\alpha} \tag{21}$$

Let $\boldsymbol{\alpha}_0$ be the normalized current coefficients of a configuration that we will take as a reference. The objective function for the power consumption (P) is defined as the ratio between the power of the configuration under study versus the power, $P_{avg,0}$, of the reference input $\boldsymbol{\alpha}_0$.

$$P(\boldsymbol{\alpha}) = \frac{P_{avg}}{P_{avg,0}} = \frac{\boldsymbol{\alpha}^{\mathrm{T}}\mathbf{Z}_c\boldsymbol{\alpha}}{\boldsymbol{\alpha}_0^{\mathrm{T}}\mathbf{Z}_c\boldsymbol{\alpha}_0} \tag{22}$$

We consider as reference the phased-array stimulation (PA) (van den Honert & Kelsall, 2007). Specifically, if $\mathbf{v}_k = (0, \dots, 1, \dots, 0)$ is the voltage pattern of the kth channel of the PA, the normalized current pattern of this channel is given by $\boldsymbol{\alpha}_{\mathrm{PA}} \equiv \boldsymbol{\alpha}_0 = N\left(J^{-1}_{max}\mathbf{Z}_c^{-1}\mathbf{v}_k\right)$, where J_{max} is the maximum current density in any VN corresponding to the input $\mathbf{Z}_c^{-1}\mathbf{v}_k$. From now on $P_{avg,0}$ becomes $P_{avg,\mathrm{PA}}$.

This objective function measures the power consumed in the perilymph by a CI fed by a current pattern $\boldsymbol{\alpha}$, compared to the power consumed by a phased-array stimulation. Note that this expression is independent of the particular waveform of the input $i_{unit}(t)$; it only depends on the profile of currents feeding the electrodes, $\boldsymbol{\alpha}$, and the resistive matrix $\mathbf{Z}_c$.

The expression (19) gives us the power dissipated in the electrolyte and tissues. However, this is only a portion of the total power consumed by a CI. A complete study should include the consumption associated with the double layer, but in that case the objective function would no longer be independent of $i_{unit}(t)$. A comparative study between the power consumed by the electrodes with and without taking into account the double layer is shown in Appendix.

Furthermore, the coil, processor and other electronic components consume a significant portion of power that has not been taken into account in the design of our target function. The power consumed by these elements depends on the particular CI manufacturer and model under consideration. Currently, we do not possess the necessary data, and as a result, we were unable to incorporate it into this study. Should such data become available, we would be able to adjust the power objective function to accommodate this additional power.

3.5. Multiobjective optimum design method

When optimizing two or more objective functions, a multiobjective optimization is required when they are in conflict (Deb, 2001); improving the optimized value of one objective function is only possible if worsening the value of other optimized objective function. As is our case, improving the focusing is possible only when worsening power consumption (alternatively improving the value of power consumption

is possible when worsening focusing). Therefore, in a multiobjective optimization procedure instead of a single optimum solution, it appears a set of equally optimum solutions called non-dominated solutions, which belong to the so called Pareto set (the objective function values belonging to the Pareto set were called Pareto front). In this work, the multiobjective optimization procedure aims to determine the non-dominated solutions (given each by its profile of currents feeding the electrodes) to achieve the maximum possible focusing for a given power consumption, or equivalently, to achieve the minimum power consumption for a given focusing.

Since the late nineties and first years of 2000s, efficient evolutionary algorithms for multiobjective optimization have been developed (Emmerich & Deutz, 2018) and applied in many real world applications (Coello, VanVeldhuizen, & Lamont, 2007; Greiner, Periaux, Quagliarella, Magalhaes-Mendes, & Galván, 2018), solving computational engineering problems (Greiner, Gaspar-Cunha, Hernandez-Sosa, Minisci, & Zamuda, 2022; Greiner, Periaux, Emperador, Galván, & Winter, 2017), as e.g. biomedical engineering applications (Carbonaro, Lucchetti, Audenino, Gries, Vaughan et al., 2023), and particularly for cochlear implant optimum design (de Miguel, Escobar, Greiner, & Ramos-Macías, 2018). Those population based global optimization methods are capable to obtain the whole set of non-dominated solutions in a single run of the algorithm without any other requirement to the objective function than being accurately computable (e.g. neither continuity nor differentiability conditions were needed, neither further computations of first nor second derivatives), what has fostered their successful application in real-world problems (Osaba et al., 2021).

Among the state of the art multiobjective evolutionary algorithms to solve two objective optimization problems, we use the most cited and applied (as in Deb 2023): the Non-dominated Sorting Genetic Algorithm NSGA-II (Deb, Pratap, Agarwal, & Meyarivan, 2002). It uses a selection based on non-dominated set ordering, and inside each non-dominated set, a crowding distance to foster diversity of solutions in the functional space; as well as simulated binary crossover (SBX) and polynomial mutation for real variable problems, as it is our case. The NSGA-II implementation of the Platyplus framework (Hadka, 2024) has been used in this manuscript. It is a recognized and used framework by the evolutionary algorithms scientific community, as seen, e.g. in Brockhoff and Tušar (2019). In this manuscript, objective functions $F_c(\boldsymbol{\alpha})$ (focusing) and $P(\boldsymbol{\alpha})$ (power consumption) as described in previous Section 3.4, were simultaneously optimized, maximizing focusing and minimizing power consumption, respectively; therefore, the set of non-dominated solutions towards the lower right part of the functional space is searched.

As previously suggested and demonstrated in the efficient resolution of certain engineering problems (such as structural frame optimization (Greiner, Emperador, & Winter, 2004), in noise barrier shape optimization (Toledo, Aznárez, Greiner, & Maeso, 2017), or in high-speed railway train timetable rescheduling (Ding et al., 2024)), inserting a high-quality solution into the initial population of the multiobjective evolutionary algorithm could enhance the non-dominated final designs. Recent research has demonstrated the effectiveness of this idea on various multiobjective mathematical benchmarks in enhancing the quality of the final front, even when only a single corner solution was used (Gong, Nan, Pang, Zhang, & Ishibuchi, 2023).

Here, we adopt this approach and propose a memetic algorithm for the purpose of obtaining high-quality solutions to each individual objective fitness function (focusing F_c, and power consumption P). Specifically, the methodology involves the integration of a differential evolution (DE) (Price, 2013; Virtanen, Gommers, Oliphant et al., 2020) with the L-BFGS-B deterministic optimization technique (Zhu, Byrd, Lu, & Nocedal, 1997). To the best of the authors' knowledge, this approach has not been previously proposed, evaluated or demonstrated for the purpose of injecting high quality solutions into a multiobjective optimization procedure. The implementation of the Python SciPy framework (Virtanen et al., 2020) has been used in this manuscript.

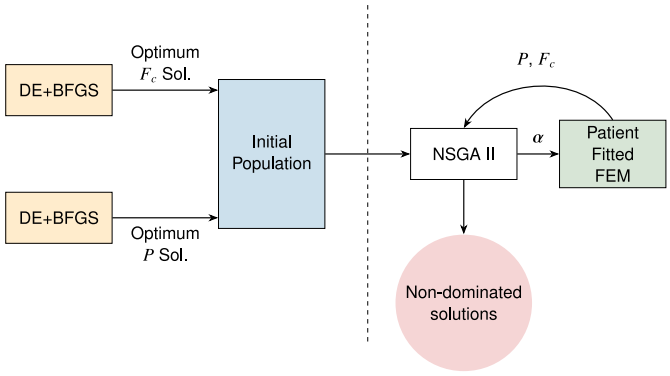

Fig. 6. Flowchart of the multiobjective optimization.

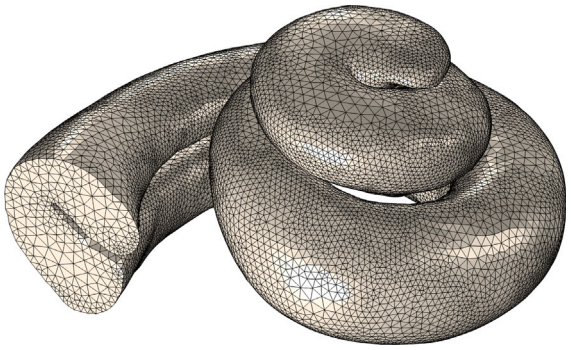

Fig. 7. Mesh of the Cochlea 1.

This method is referred as follows as DE+BFGS Injected. This has allowed us to obtain best individuals of each fitness function and insert them into the initial population of the multiobjective algorithm. Key advantages of this approach will be discussed in the next Section 4. Particularly, Section 4.3 shows experimental results comparing a Random initial population, the DE+BFGS Injected strategy, and to further investigate the influence of the BFGS stage, a DE strategy without BFGS. Fig. 6 shows a flowchart of the described optimization process, where the left part represents the solutions injected into the initial population and the right part represents the multiobjective optimization process.

4. Test cases and experimental results

In the first Section 4.1 a description of the implemented test cases is given. In Section 4.2 detail of optimization methods is described. Section 4.3 presents a comparison of initial population strategies. Then, experimental results of optimum focusing are presented in Section 4.4. Finally, experimental results of multiobjective optimization are shown in Section 4.5.

4.1. Description of test cases

Two FEM cochlear geometries with perimodiolar insertion of the electrode array were taken into account; they are named Cochlea 1 and Cochlea 2. Both geometries are based on meshes taken from the procedure described in the work of Mangado et al. (2018). A representation of the mesh of Cochlea 1 is shown in Fig. 7.

To solve the model described in Section 3.3, we have used *COMSOL Multiphysics®* 5.6. Table 1 shows the dimensions of the cochleas, and the number of quadratic tetrahedral elements and degrees of freedom for each FEM mesh. Each evaluation takes an average of 462 s in an Intel Core i9–10900X 3.70 GHz. The conductivities of each one were adjusted to a different patient transimpendance matrix following the procedure

Table 1
Spatial dimensions in mm (x, y, z), number of quadratic tetrahedral elements (N_e) and degrees of freedom (df) for each FEM mesh.

Case	x	y	z	N_e	df
Cochlea 1	6.654	7.796	4.289	946 110	1374899
Cochlea 2	6.481	6.567	3.707	800 747	1170224

Table 2
Optimum conductivities σ_{opt} in $S\,m^{-1}$ and R (Eq. (7)) of the two cochlear models.

Case	σ_{ext}	σ_{bone}	σ_{per}	R
Cochlea 1	0.4393	0.0628	1.565	969.0
Cochlea 2	1.1265	0.0944	1.982	1161.3

described in Section 3.2. The values of σ_{opt} and R (Eq. (7)) of each model are shown in Table 2. If we take into account that R of Table 2 provides a global error, and that the transimpedance matrix has 22×22 elements, the average error per element is 2.0 Ω for Cochlea 1 and 2.4 Ω for Cochlea 2.

4.2. Description of optimization procedure

After defining the model, evaluations of the objective functions are calculated by following the steps outlined in Section 3.4. Each evaluation pair (F_c and P) takes an average of 0.78 ms in an Intel Core i9–10900X 3.70 GHz.

A multiobjective optimization with NSGA-II as described in Section 3.5 was applied for each cochlear model. Standard parameters were applied: a population size of 100 individuals, SBX crossover probability of 1.0 with distribution index of 15 and polynomial mutation with mutation rate of one divided by the number of variables of the chromosome (constituted by the 22 current coefficients α of each electrode of the CI) with distribution index of 20. In the following sections, when the current coefficients α are mentioned, they are rescaled to the interval $[-1, 1]$.

As stated in Section 3.5, the initial population of the multiobjective evolutionary algorithm is injected with high quality corner solutions. These solutions are obtained by executing a memetic DE with a population size of 110 individuals and 100 generations as the stopping criterion for each objective function. After the convergence of the DE, a L-BFGS-B optimization (Virtanen et al., 2020; Zhu et al., 1997) is executed taking as initial solution the best DE individual. This process is repeated five times, and the best corner individuals are added to the initial population of the NSGA-II. This method, referred to as DE+BFGS Injected, is compared to an initial random population (referred to as Random), and to DE without the L-BFGS-B step (referred to as DE Injected) to further investigate the influence of the BFGS stage, in the following Section 4.3.

4.3. Results: Initial population strategy

Twenty-one independent runs were conducted, each consisting of 210,000 evaluations of the evolutionary algorithm. The NSGA-II was used with 2100 and 1000 generations as stopping criteria for the Random and DE Injected strategies, respectively. Some representative electrodes (3, 5, 6, 10, 14, 16 and 17) were chosen as benchmarks, for both Cochlea 1 and Cochlea 2 test cases. The hypervolume indicator (Zitzler, Thiele, Laumanns, Fonseca, & da Fonseca, 2003) was used to compare the methods, with scaling values of 110 for focusing (F) and 3 for power consumption (P), and a reference point of (2,2). The results of the Friedman test are presented Table 3, which confirms the rejection of the null hypothesis and indicates that some methods are superior to others. In all table columns, DE+BFGS Injected is the best ordered strategy, followed by Random, and ending with DE Injected.

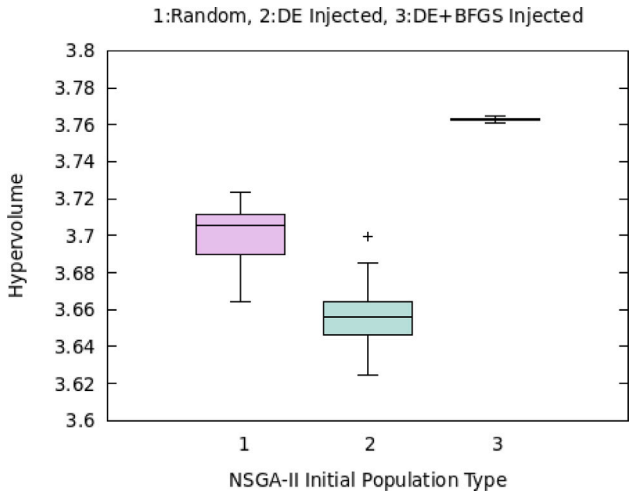

Fig. 8. Boxplot of final hypervolume of the 21 independent executions for each initial population strategy. Electrode 10. Cochlea 1.

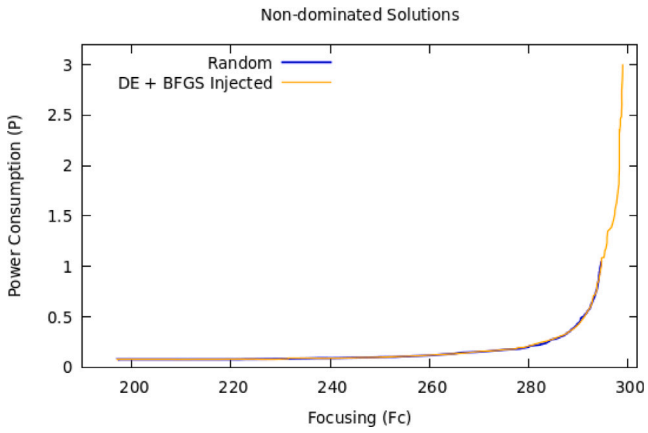

Fig. 9. Non-dominated solutions of the median execution (out of 21) ordered in terms of hypervolume. Comparing random initial population with injected DE+BFGS corner solutions. Electrode 10. Cochlea 1.

As example, Fig. 8 shows a boxplot of the final hypervolume distribution of the methods for Electrode 10 of Cochlea 1, indicating that DE+BFGS performs better than Random and the latter is better than DE Injected. Table 4 presents the results of the Bergmann-Hommel's posthoc procedure (Garcia & Herrera, 2008), where paired comparisons with a p-value lower than 0.05 are considered significant. Therefore, it is confirmed that the best ordered algorithm in the Friedman test, the DE+BFGS injected solution outperforms all the other compared algorithms. Additionally, the Random initial population is better or not worse than the DE injected solution. As example, Fig. 9 compares the median non-dominated fronts (the eleventh front ordered in terms of the hypervolume indicator) of Random and DE+BFGS injected methods for Electrode 10 of Cochlea 1. It is evident that the most challenging non-dominated solutions to attain in this problem are those located in the upper right part of the front; i.e., the solutions with higher focusing. These solutions are only attained in the yellow line (belonging to the DE+BFGS injected method) and are the ones that determine the higher value of hypervolume than the other methods, as shown in Fig. 8.

The non-dominated front length of the median front (eleventh front ordered in terms of HV out of twenty-one runs) of the Random strategy was compared in percentage with the DE+BFGS Injected strategy in Table 5. In all cases, the non-dominated front length of the Random strategy is shorter, ranging from 36.4% to 62.9% in the electrodes of Cochlea 1, and from 51.5% to 86.5% in the electrodes of Cochlea 2

Table 3
Friedman Test: Average rankings of the algorithms based on hypervolume final distribution. Comparing initial population strategies in Electrodes 3, 5, 6, 10, 14, 16 and 17. Cochlea 1 and Cochlea 2.

Electrode Number (Cochlea 1)	El-3	El-5	El-6	El-10	El-14	El-16	El-17
DE+BFGS Injected	1.00	1.00	1.00	1.00	1.00	1.00	1.00
Random	2.00	2.00	2.43	2.00	2.00	2.05	2.10
DE Injected	3.00	3.00	2.57	3.00	3.00	2.95	2.90
p-value	7.83×10^{-10}	7.83×10^{-10}	1.30×10^{-7}	7.83×10^{-10}	7.83×10^{-10}	2.00×10^{-9}	4.65×10^{-9}
Electrode Number (Cochlea 2)	El-3	El-5	El-6	El-10	El-14	El-16	El-17
DE+BFGS Injected	1.00	1.00	1.19	1.00	1.00	1.00	1.10
Random	2.00	2.00	1.95	2.10	2.00	2.05	2.14
DE Injected	3.00	3.00	2.86	2.90	3.00	2.95	2.76
p-value	7.83×10^{-10}	7.83×10^{-10}	4.48×10^{-7}	4.65×10^{-9}	7.83×10^{-10}	2.00×10^{-9}	3.36×10^{-7}

Table 4
Adjusted *p*-values. Bergmann-Hommel's posthoc procedure. Comparing initial population strategies in Electrodes 3, 5, 6, 10, 14, 16 and 17. Cochlea 1 and Cochlea 2.

Electrode Number (Cochlea 1)	El-3	El-5	El-6	El-10	El-14	El-16	El-17
DE In.vs. DE+BFGS In.	2.74×10^{-10}	2.74×10^{-10}	1.06×10^{-6}	2.74×10^{-10}	2.74×10^{-10}	7.53×10^{-10}	2.02×10^{-9}
Random vs. DE+BFGS In.	1.19×10^{-3}	1.19×10^{-3}	3.67×10^{-6}	1.19×10^{-3}	1.19×10^{-3}	6.87×10^{-4}	3.87×10^{-4}
Random vs. DE In.	1.19×10^{-3}	1.19×10^{-3}	0.64	1.19×10^{-3}	1.19×10^{-3}	3.37×10^{-3}	8.71×10^{-3}
Electrode Number (Cochlea 2)	El-3	El-5	El-6	El-10	El-14	El-16	El-17
DE In.vs. DE+BFGS In.	2.74×10^{-10}	2.74×10^{-10}	1.99×10^{-7}	2.02×10^{-9}	2.74×10^{-10}	7.53×10^{-10}	1.99×10^{-7}
Random vs. DE+BFGS In.	1.19×10^{-3}	1.19×10^{-3}	3.37×10^{-3}	3.87×10^{-4}	1.19×10^{-3}	6.87×10^{-4}	6.87×10^{-4}
Random vs. DE In.	1.19×10^{-3}	1.19×10^{-3}	1.36×10^{-2}	8.71×10^{-3}	1.19×10^{-3}	3.37×10^{-3}	4.49×10^{-2}

Table 5
Comparing median non-dominated front length of Random initial population NSGA-II versus DE+BFGS Injected in Electrodes 3, 5, 6, 10, 14, 16 and 17. Cochlea 1 and Cochlea 2. Length of DE+BFGS Injected strategy is 100%.

Electrode Number (Cochlea 1)	El-3	El-5	El-6	El-10	El-14	El-16	El-17
Random	56.6%	36.4%	38.2%	62.5%	44.3%	54.7%	62.9%
Electrode Number (Cochlea 2)	El-3	El-5	El-6	El-10	El-14	El-16	El-17
Random	58.1%	78.1%	51.5%	86.5%	67.7%	80.8%	83.8%

(being 100% the length of the DE+BFGS Injected non-dominated front, in each case). As further analysis, the improvements in terms of HV shown in the previous paragraph by the DE+BFGS Injected strategy are mainly explained by the higher length of the non-dominated front.

To summarize the results of this Section 4.3 in this cochlear implant multiobjective optimization problem: they show a robust behavior in Cochlea 1 and Cochlea 2 and their electrodes, where the proposed algorithm (DE+BFGS Injected) consistently outperforms the Random initial population, allowing to obtain enhanced non-dominated solutions. In terms of the handled problem it is particularly relevant to be able to obtain a larger (extended) non-dominated front with higher focusing solutions, which is associated with better hearing frequency discrimination and therefore, an improvement in hearing quality could potentially be achieved with the method proposed in Section 3.5.

4.4. Results: Optimum focusing solutions

First, we present results of the optimum focusing (OF) solutions attained, comparing them with the phased-array (PA) and monopolar (MP) stimulation.

Figs. 10 and 11 represent current densities j^n_{max}. They include seven representative electrodes out of the twenty-two constituting the cochlear implant distributed along the cochlea, in Cochlea 1 and Cochlea 2, respectively. The value of M of these electrodes varies from 5 to 10, being M the cardinal of the VNs closer to electrode k than to the other electrodes, as explained in Section 3.4.1. A total of N_n equal to 151 VNs were distributed throughout the cochlea in each test case, as shown in the abscissa axis of the figures. It is clearly appreciable how the optimum focusing solutions (black lines) are able to fit properly towards the objective functions (red lines), being those optimum profiles narrower than phased-array stimulation (green lines) and they narrower than the monopolar (magenta lines) in all cases.

Corresponding values of the objective functions for focusing F_c and power consumption P are shown in Table 6 for Cochlea 1 and Cochlea 2. As expected, the higher the focusing, the higher the power consumption. In all cases focusing and power consumption increase from monopolar to phased-array and from phased-array to optimum focusing solutions.

From all these results, it has been evidenced the capability of the methodology to improve phased-array stimulation in CI for maximizing the focusing F_c.

4.4.1. Extracting design principles

The analysis of optimum attained solutions could lead to interesting design principles, as have being exposed in optimum design of engineering problems through the innovization principle in Deb, Bandaru, Greiner, Gaspar-Cunha, and Tutum (2014). With this purpose for focusing maximization, the optimum values of the current coefficients α of each electrode from 3 to 17 have been superimposed in Figs. 12 and 13, respectively for Cochlea 1 and Cochlea 2. In each case, the relative position 0 belongs to each central active electrode.

As observed in both figures, a clear shared pattern emerges that allows the focusing maximization: the previous and posterior adjacent values (relative positions −1 and +1, respectively) with respect to the central active electrode (relative position 0) are negative and decreased values; the next adjacent values (relative positions −2 and +2, respectively) are positive and again decreased values; and so on, alternating signs and continuing in the decrement of the values of the coefficients. As relevant shared values of the pattern in Cochlea 1 and Cochlea 2, we choose the median of the distribution of the values belonging to relative positions: −4, −3, −2, −1, 0, +1, +2, +3, +4. These median patterns are shown in Table 7. Distribution of current coefficients of this median pattern common to all electrodes versus those of the phased-array stimulation (e.g. of Electrode 10) of both test cases are shown in Fig.

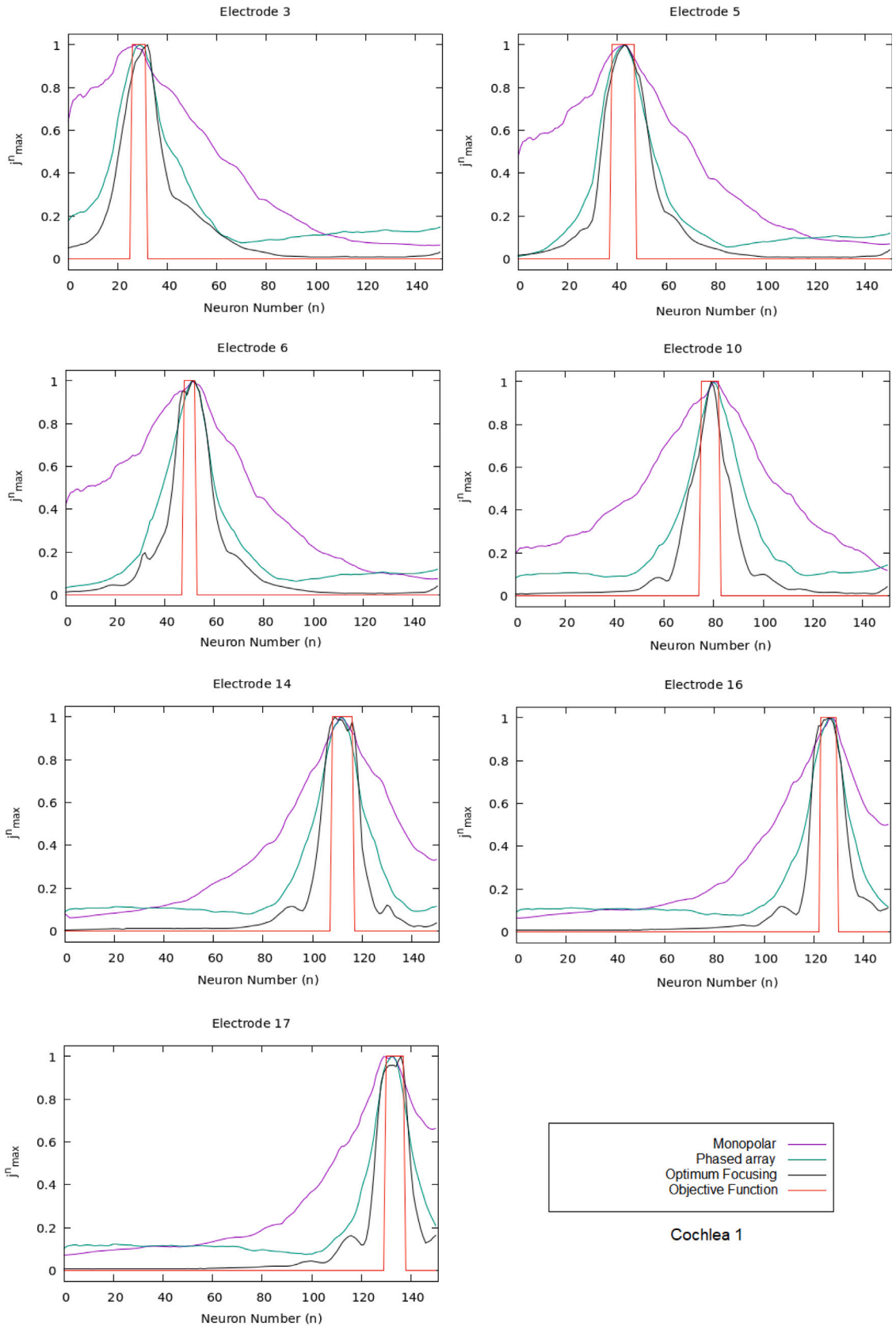

Fig. 10. Distribution of current density j^n_{max} for OF, MP and PA. compared with the target objective function profile (in red). Electrodes 3, 5, 6, 10, 14, 16 and 17 of Cochlea 1.

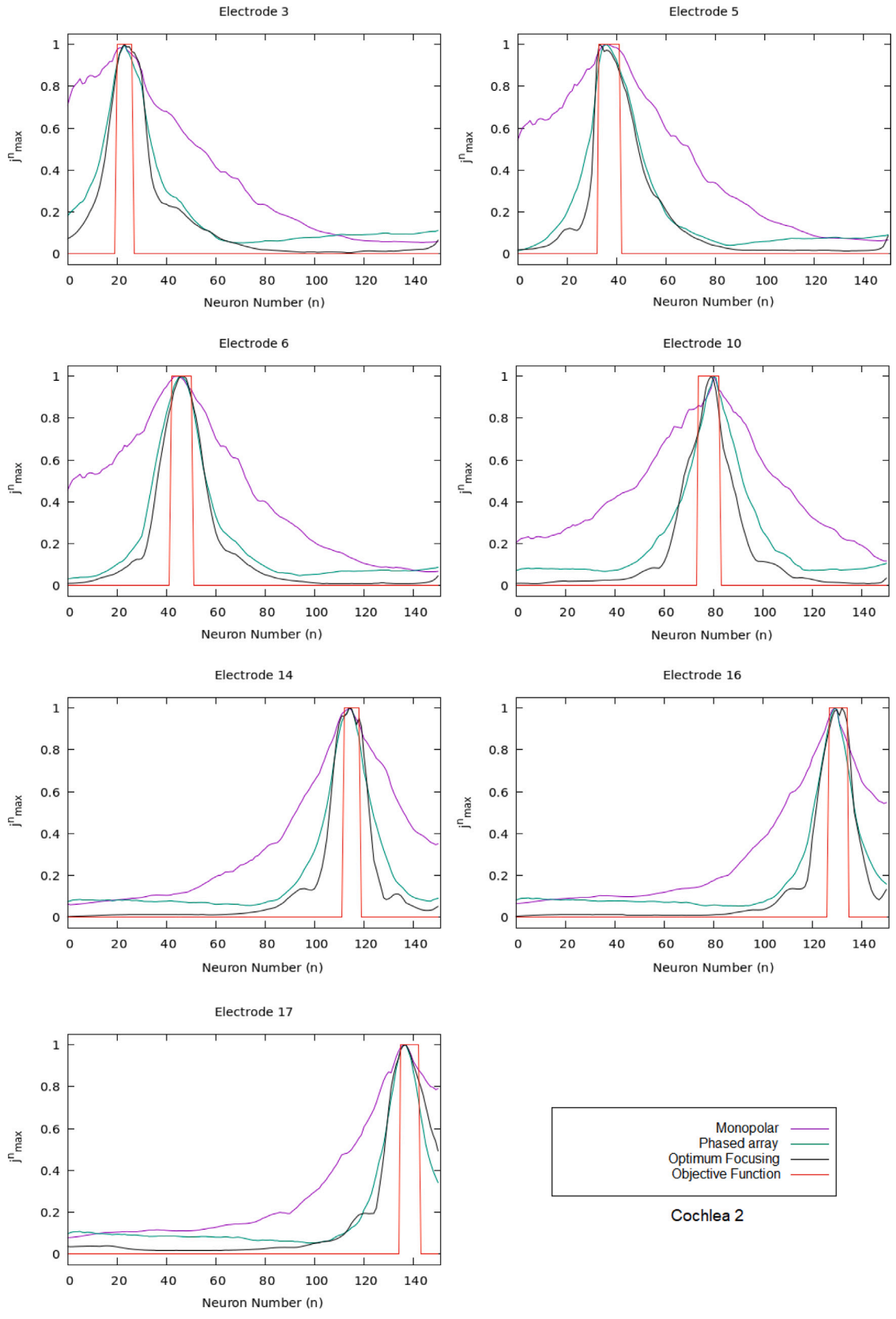

Fig. 11. Distribution of current density j^n_{max} for OF, MP and PA. compared with the target objective function profile (in red). Electrodes 3, 5, 6, 10, 14, 16 and 17 of Cochlea 2.

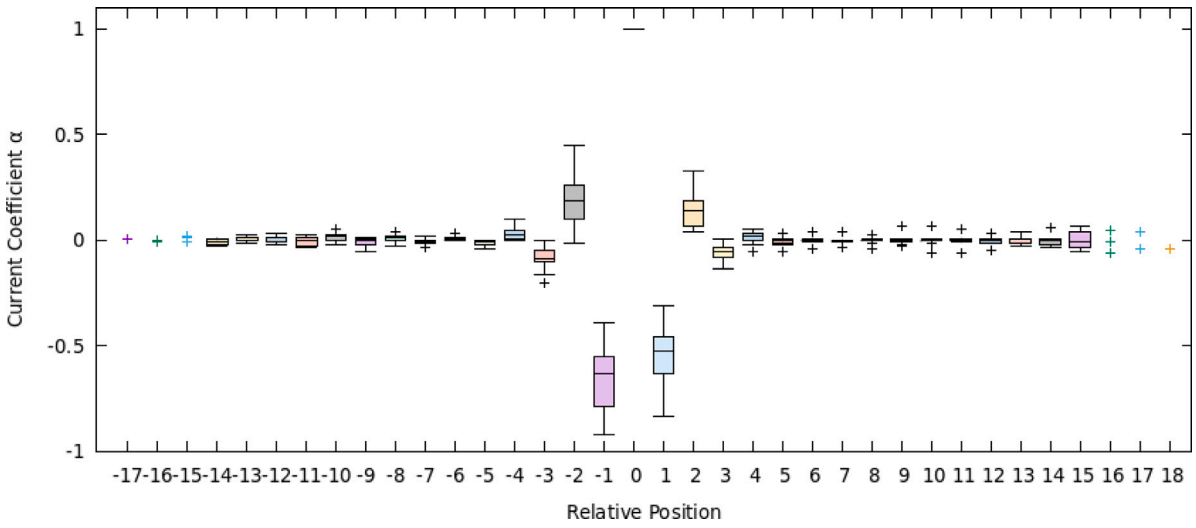

Fig. 12. Distribution of current coefficients α of the OF solutions (rescaled to interval $[-1, 1]$) for electrodes 3 to 17 of Cochlea 1. Relative numbering of the electrodes has been adopted, so that the maximum α is associated with relative position 0.

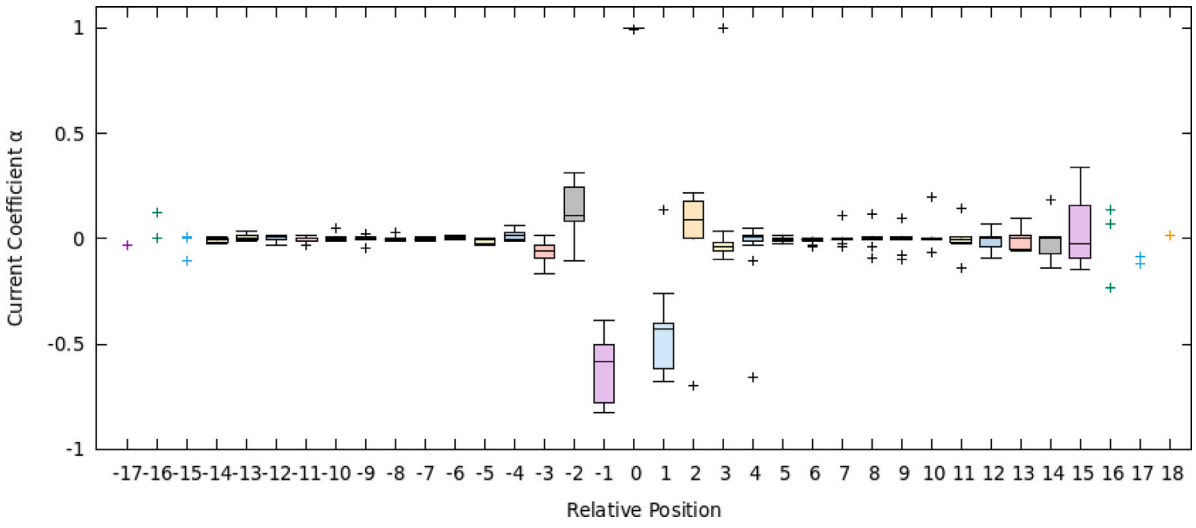

Fig. 13. Distribution of current coefficients α of the OF solutions (rescaled to interval $[-1, 1]$) for electrodes 3 to 17 of Cochlea 2. Relative numbering of the electrodes has been adopted, so that the maximum α is associated with relative position 0.

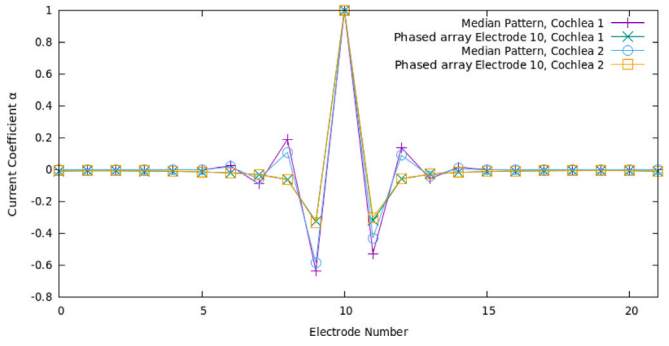

Fig. 14. Current coefficients α (rescaled to interval $[-1, 1]$) of the median pattern compared with PA. Example for electrode 10, Cochlea 1 and Cochlea 2.

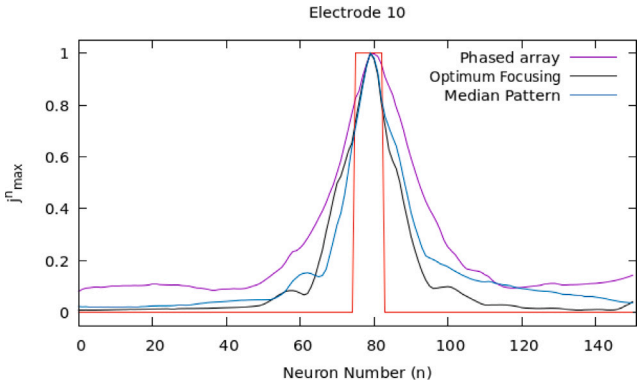

Fig. 15. Distribution of current density j^n_{max} for median pattern, OF and PA. compared with the target objective function profile (in red). Electrode 10 of Cochlea 1.

14. A clear difference emerges between both configurations of Cochlea 1 and Cochlea 2 handled in this manuscript, as in the phased-array stimulation only negative values of the coefficients remain, without sign oscillation.

If using those pattern values as current stimulation in the CI, Figs. 16 and 17 show that the focusing slightly diminishes with respect to

Table 6
Optimum values of the objective functions of focusing, F_c, and power, P, for Cochlea 1 and Cochlea 2. Electrodes 3, 5, 6, 10, 14, 16 and 17.

Electr.	Stimul.	Cochlea 1		Cochlea 2	
		F_c	P	F_c	P
3	MP	269.61	0.158	272.92	0.120
	PA	292.76	1.000	293.98	1.000
	OF	297.29	2.920	296.39	2.729
5	MP	267.08	0.215	268.69	0.193
	PA	291.10	1.000	294.40	1.000
	OF	293.41	3.365	296.53	3.060
6	MP	266.57	0.232	269.32	0.215
	PA	293.09	1.000	294.49	1.000
	OF	296.66	4.774	296.43	2.234
10	MP	266.57	0.274	268.86	0.302
	PA	290.26	1.000	290.57	1.000
	OF	295.01	3.003	295.20	2.611
14	MP	277.74	0.243	279.23	0.243
	PA	293.41	1.000	295.12	1.000
	OF	298.08	6.465	297.82	3.667
16	MP	281.97	0.259	281.90	0.281
	PA	295.43	1.000	293.60	1.000
	OF	298.79	4.052	297.30	2.863
17	MP	280.21	0.280	281.67	0.311
	PA	293.34	1.000	292.88	1.000
	OF	297.81	3.564	293.63	1.831

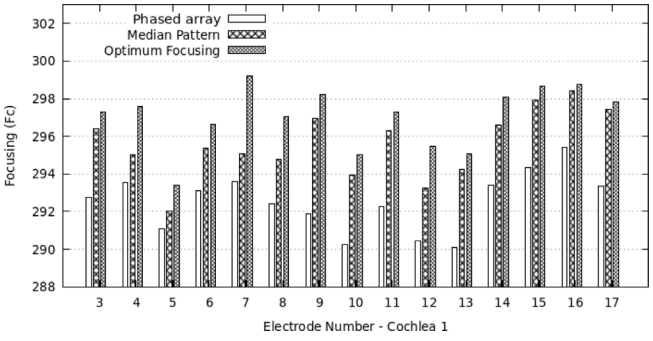

Fig. 16. Focusing values (F_c) of median pattern versus OF and PA. Electrodes 3 to 17 of Cochlea 1.

the optimum solution. However, this median pattern is able to improve the focusing of the phased-array stimulation solutions consistently in both test cases Cochlea 1 and Cochlea 2, with the only exception of electrodes 3, 4, 5 and 6 of Cochlea 2. As seen in relative position +15 of Fig. 13, the dispersion of solutions in this position is larger in Cochlea 2 than in Cochlea 1. These values belong to electrodes 3, 4, 5 and 6 of Cochlea 2, whose larger variability decreases the focusing of the median pattern in Cochlea 2. Therefore, from these results, the pattern of current coefficients is more reliable when their boxplots in the extreme ranges remain with low dispersion.

The direct relationship between the focusing F_c and narrowness of the profile of the current densities j^n_{max} along the VNs, as shown previously in Figs. 10 and 11, can be observed in Fig. 15. When comparing phased-array stimulation (magenta), median pattern (blue) and optimum focusing (black) curves, the median pattern clearly outperforms phased-array stimulation.

From all these results, it has been evidenced the capability of the methodology to lead to design principles for improving phased-array stimulation to maximize focusing in CI: a pattern with alternating signs and decreased values of the current coefficients.

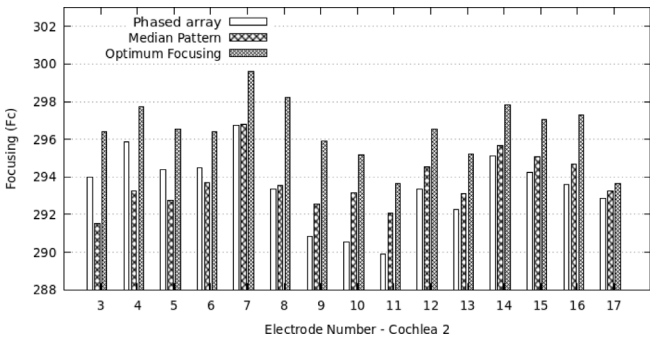

Fig. 17. Focusing values (F_c) of median pattern versus OF and PA. Electrodes 3 to 17 of Cochlea 2.

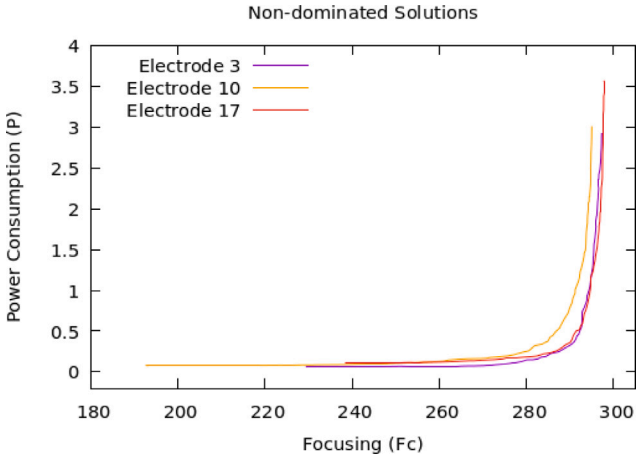

Fig. 18. Non-dominated solutions, maximizing focusing F_c and minimizing power consumption P, of Electrodes 3, 10, and 17 of Cochlea 1.

4.5. Results: Multiobjective optimization solutions

The outcome of the multiobjective optimization is the set of non-dominated solutions of maximum focusing F_c and minimum power consumption P. All of them are equally optimum from the mathematical point of view.

In Fig. 18 for Cochlea 1 these solutions are represented as lines for some chosen electrodes (3, 10, 17). While the lower left extreme of each line represents the solution with lower power consumption P, the upper right extreme of each line represents the solution with higher focusing F_c. The line represents the values of maximum focusing for each value of power consumption. Alternatively, the line also represents the values of minimum power consumption for each value of focusing.

In Fig. 19 we can zoom in to compare monopolar (crosses) and phased-array (asteriscs) solutions versus the non-dominated solutions (line). Clearly, there are non-dominated solutions that improve simultaneously F_c and P in each case (see all those solutions represented by the line that are located lower and more to the right). Therefore, the multiobjective optimization provides a set of optimum solutions that improve the phased-array stimulation in both objective functions for all cases.

As an example, Fig. 20 shows the case of electrode 10 of Cochlea 1. Three representative non-dominated solutions named Solution 1, 2 and 3 were selected. Solution 1 improves the phased-array stimulation in both objective functions F_c (291.20 is higher than 290.26) and P (0.96645 is lower than 1.0). Solution 3 improves the monopolar solution in both objective functions (279.20 is higher than 266.57 in focusing, and 0.24269 is lower than 0.27396 in power consumption).

Table 7
Median pattern current coefficients $\boldsymbol{\alpha}$ rescaled to interval $[-1, 1]$.

Test case	−4	−3	−2	−1	0	+1	+2	+3	+4
Cochlea 1	0.02398	−0.08982	0.18915	−0.63481	1.0000	−0.52722	0.13819	−0.05752	0.01610
Cochlea 2	0.01712	−0.05814	0.10859	−0.58626	1.0000	−0.43001	0.08941	−0.04082	0.00710

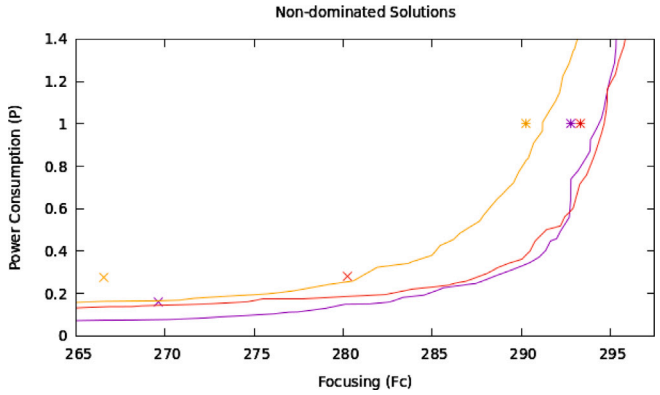

Fig. 19. Zoom of Fig. 18 including MP (crosses) and PA (asteriscs).

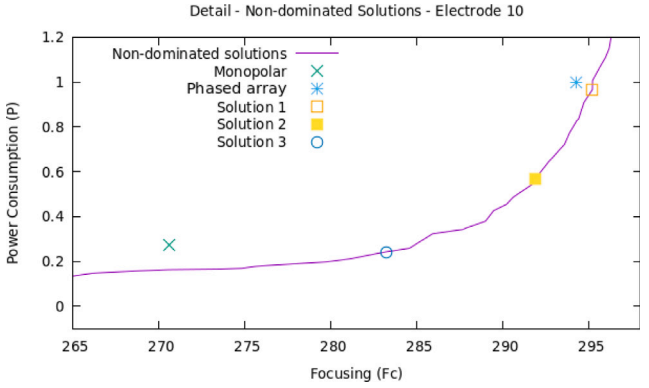

Fig. 20. Some selected representative non-dominated solutions: Solution 1, Solution 2 and Solution 3 of Electrode 10 of Cochlea 1.

An intermediate Solution 2 attains almost the focusing of the phased-array stimulation (value of 287.88 versus 290.26) with only half of the power consumption (0.56897 versus 1.0). All the values of the objective functions of these solutions are shown in Table 8. This case is an example that shows the usefulness of the proposed multiobjective optimization methodology for improving CI in terms of both focusing and power consumption, simultaneously.

Fig. 21 shows the direct relationship between the focusing F_c and the narrowness of the profile of the current densities j^n_{max} along the VNs for Solutions 1 (black), 2 (green) and 3 (magenta). As can be seen, larger values of F_c imply higher narrowness.

In Figs. 22, 23 and 24, we compare current coefficients $\boldsymbol{\alpha}$ of representative non-dominated Solutions 1, 2 and 3 with respect to monopolar, phased-array stimulation and optimum focusing solutions, respectively. Note in Figs. 22 and 23 that only slight changes in $\boldsymbol{\alpha}$ improve both objective functions.

From all these results, it was shown the capability of the proposed methodology to lead to non-dominated solutions to improve simultaneously F_c and P, even with respect to the phased-array stimulation.

Table 8
Multiobjective optimization: non-dominated Solutions 1, 2 and 3. Electrode 10. Cochlea 1.

Electrode	Solution	F_c	P
	MP	266.57	0.27396
	PA	290.26	1.00000
10	Solution 1	291.20	0.96645
	Solution 2	287.88	0.56897
	Solution 3	279.20	0.24269

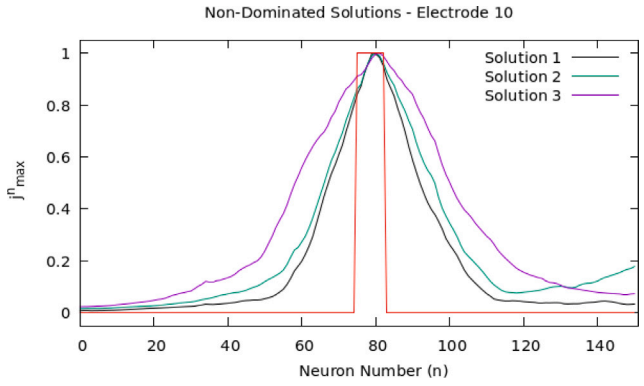

Fig. 21. Distribution of current density j^n_{max} for non-dominated solutions: Solution 1, Solution 2 and Solution 3, compared with the target objective function profile (in red). Electrode 10 of Cochlea 1.

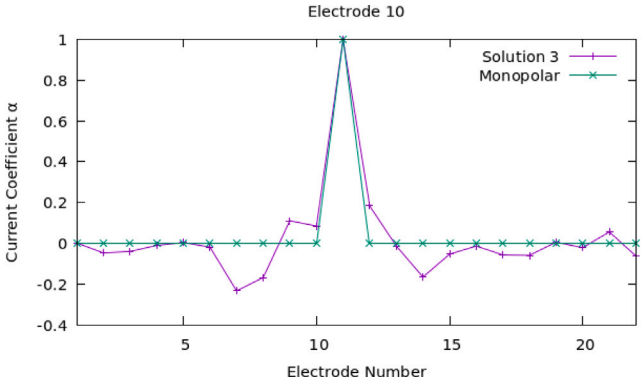

Fig. 22. Current coefficients $\boldsymbol{\alpha}$ (rescaled to interval $[-1, 1]$) of Solution 3 (which improves simultaneously F_c and P of MP), compared with MP. Example for electrode 10, Cochlea 1.

5. Discussion

5.1. Threshold current density

As previously explained, one of our objectives has been to construct an objective function, F_c, (Eq. (18)) that allows obtaining a stimulation pattern that maximizes the focusing. Furthermore, F_c allows us to compare the degree of focusing of other stimulation patterns, such as monopolar (MP) or phased-array (PA), as shown in Figs. 10 and 11. Therefore, the proposed focusing F_c has been shown in Sections 4.4 and 4.5 to be effective in terms of the assessment of the focusing of the current density distribution, and its maximization attains improved

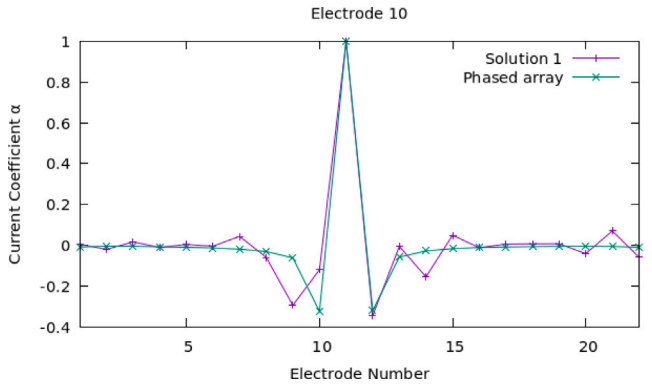

Fig. 23. Current coefficients $\boldsymbol{\alpha}$ (rescaled to interval $[-1, 1]$) of Solution 1 (which improves simultaneously F_c and P of PA), compared with PA. Example for electrode 10, Cochlea 1.

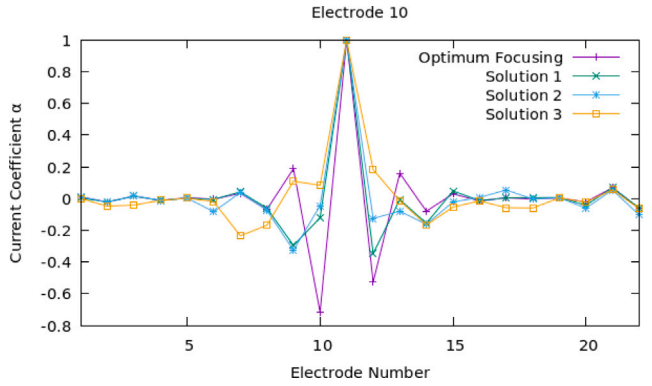

Fig. 24. Current coefficients $\boldsymbol{\alpha}$ (rescaled to interval $[-1, 1]$) of non-dominated solutions: Solution 1, Solution 2 and Solution 3, compared with OF. Example for electrode 10, Cochlea 1.

profiles of the current density, more narrow and concentrated in the target area. Our interest lies in determining whether one stimulation pattern is more focusing than another, but not on knowing whether or not the hearing threshold level is reached. This threshold is determined by J_{th}, but this parameter is difficult to calculate and depends on the state of preservation of the auditory nerve, and therefore on the patient under consideration. Furthermore, it must be taken into account that the value of J_{th} given in Eq. (6) is deduced from the experimental law (5), and is therefore subject to inaccuracies, as it is shown in Joucla, Branchereau, Cattaert, and Yvert (2012).

Some authors (see, for example, Nowak and Bullier 1996 and Mahnam, Hashemi, and Grill 2008) consider a slightly different version of Eq. (6), so that, $I_{th} = I_0 + K_e r^2$, where I_0 is the current necessary to activate the neuron when the electrode and the neuron are almost in contact. In this case, the threshold current density would no longer be constant, but rather varies with the distance from the source, although for large distances it coincides with the value given in Eq. (6).

5.2. Comparing with a model based on active neurons

Our model uses passive VNs to measure current density over the positions that real neurons would occupy in a biological model. In this section we analyze whether the use of active neurons maintains the same focus ranking as that obtained using passive neurons. To this end, we will utilize the neuronal model developed by Ashida and Nogueira (2018), whereby activation is governed by the potentials at the nodes of Ranvier induced by the currents injected into the electrodes. We have considered three different current patterns for the simulation: monopolar (MP), phased array (PA) and optimum focusing (OF), with waveform as shown in Fig. 1. The amplitudes of the currents injected by the electrodes are $\boldsymbol{I} = I_0\boldsymbol{\alpha}'$, where $\boldsymbol{\alpha}' = (\alpha_i')$ is the current pattern (see Section 3.4.1), normalized so that $\max(\alpha_i') = 1$, and I_0 is a scaling factor, which coincides with maximum current amplitude present in the electrode array.

Fig. 25, corresponding to stimulation centered on electrode 4 (top) and 11 (bottom) of Cochlea 1, shows the scaling factor I_0 (in mA) in terms of the number of the neuron. As expected, I_0 increases with the distance of the neurons from the target region. The narrower the U-shaped profile of the curve, the more focused the proposed pattern of currents. The graphs show that according to the results obtained with active neurons, the least focusing stimulation is MP, followed by PA and the most focusing is OF. These graphs also show that the threshold values of I_0 required to evoke an action potential in the neurons closest to the target region are, in increasing order, MP, PA and OF. This means that the power required to stimulate the target neurons follows the same order. These outcomes are in agreement with the results obtained using passive neurons. Although only the responses for a stimulus centered on an apical and central electrode of Cochlea 1 are shown in Fig. 25, similar results were obtained for the remaining electrodes.

The CPU times for the multiobjective optimization (Section 3.5) executed on an Intel i7-10510U CPU (1.80 GHz) in a Linux Ubuntu laptop are summarized as follows: On average, each solution evaluation pair (F_c and P) requires 0.98 ms. The entire multiobjective optimization process (NSGA-II, incorporating the injection of two corner solutions into the population) takes approximately 568.1 s (9 minutes and 30 s). In contrast, the computation time needed to calculate each current pattern with active neurons is five orders of magnitude (10^5) higher than for passive neurons (see Section 4.2). Consequently, reproducing a similar optimization process as described in Section 4.2 using active neurons would require an impractical amount of time (on the order of a year), which would make it unfeasible for practical use.

5.3. Crosstalk

The increase of the focusing results in the reduction of the interaction between channels, a phenomenon known as crosstalk. The following example illustrates this issue. Fig. 26 shows the current density curves corresponding to stimulations centered on electrodes 6 and 10 at Cochlea 1 for MP and OF. The magenta and black lines at the bottom of the graph show the VNs whose current density is above the threshold current level J_{th} (green line). We see that in the situation represented in Fig. 26, crosstalk does occur when the stimulation is MP (bold magenta line), but it does not occur when the stimulation is OF. In that sense, the vector of current coefficients $\boldsymbol{\alpha}$ achieved from the optimization helps reduce crosstalk between channels by improving the focusing F_c. In Fig. 27 it is observed that with the present values of J_{max} and J_{th} no crosstalk appears. However, if J_{max} increases due to an increase in the amplitude of the input current, there will come a point where crosstalk will occur, but it would appear earlier with PA than with OF stimulation. In Figs. 26 and 27 we can also see that a current density profile with a steeper decrease as we move away from the target neurons indicates greater focusing than another profile with a smoother decrease. Regardless of the value of J_{th}, the number of excited neurons (current density greater than J_{th}) is always lower with OF stimulation than with MP (Fig. 26) or with PA (Fig. 27).

5.4. Pattern of optimal current profiles

In Section 4.4, while analyzing the best focusing designs, a pattern of alternating current signs emerged as we move away from the central electrode. This pattern was particularly noticeable where significant values were provided by up to four adjacent electrodes on either side of the central one. The current coefficients exhibited an alternating sign pattern (+, -, +, -, +) with successively decreasing

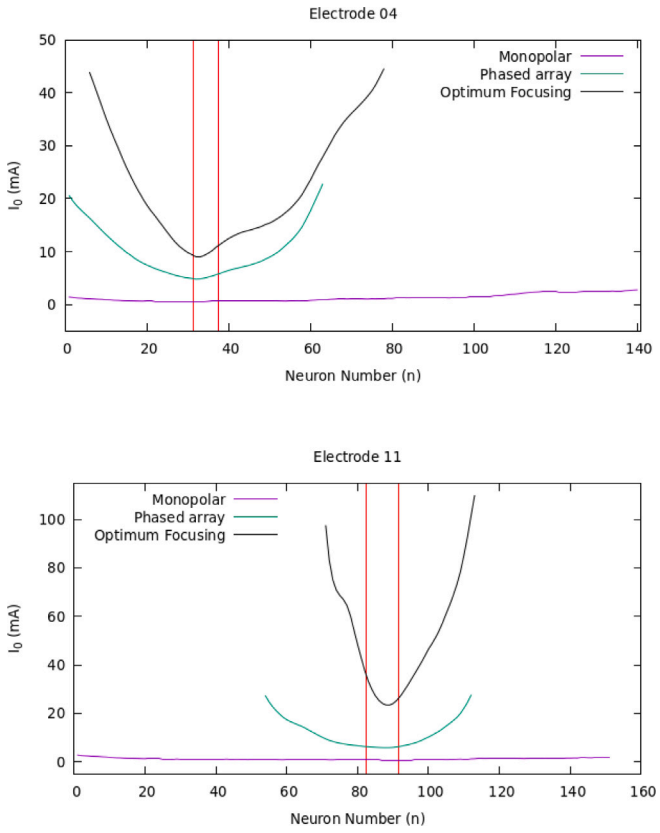

Fig. 25. Current amplitude I_0 to evoke an action potential as a function of the neuron number for MP, PA and OF patterns; Cochlea 1. Vertical lines indicate the boundaries of the neurons closest to the electrode in each figure.

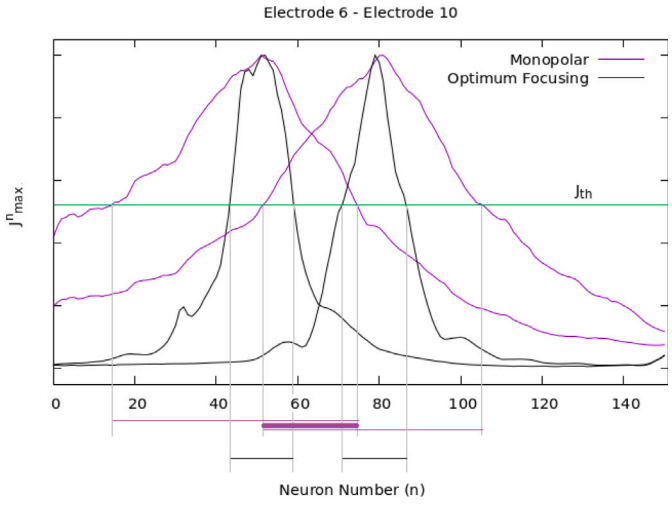

Fig. 26. Crosstalk between electrodes 6 and 10 of Cochlea 1.

values. This pattern can be compared with another recent proposal where the use of opposing signs in the current coefficients has been claimed as beneficial for reducing the spread of current along the cochlea's frequency axis (Croghan, Krishnamoorthi, & Smith, 2023). In this proposal, compensation currents are delivered with a polarity opposite to that of a primary current, and only two adjacent current coefficients are considered. Both of these coefficients have consecutive negative signs (+, -, -, 0, 0), without the characteristic alternating sign. The best proposed focusing solution, derived from the qualitative figure proposed in Croghan et al. (2023), is measured and translated into a

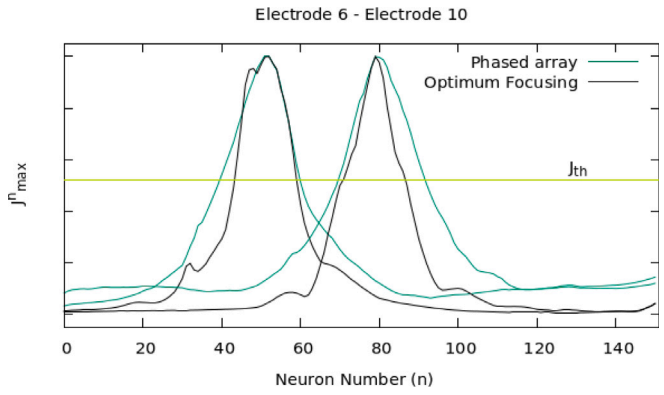

Fig. 27. Current densities of PA and OF for electrodes 6 and 10 of Cochlea 1.

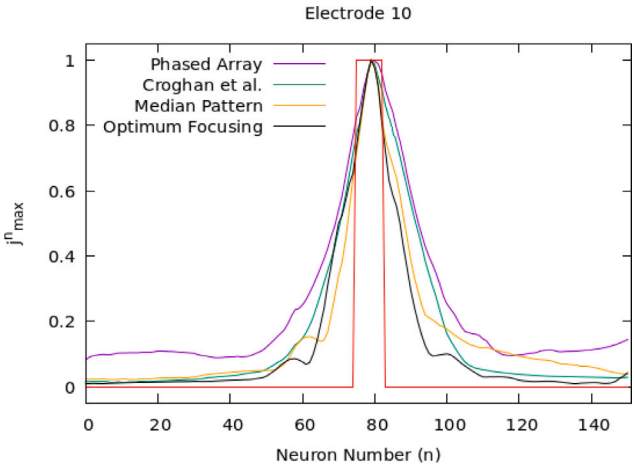

Fig. 28. Comparison of distribution of current density j^n_{max} including Croghan et al. (2023) estimation. Electrode 10 of Cochlea 1.

Table 9
Comparison of focusing F_c and power consumption P including Croghan et al. (2023) estimation. Electrode 10 of Cochlea 1.

Design	F_c	P
PA	290.26	1.00000
Croghan et al. (2023)	292.46	1.24705
Median Pattern	293.97	2.33882
OF	295.01	3.00293

set of normalized current coefficients alpha of (+1, −0.33, −0.14, with the rest of values being 0) as we move away from the central active electrode. This solution is evaluated using our objective functions for focusing (F_c) and power consumption (P). It is then compared with the phased-array, the median pattern, and the optimum focusing in Electrode 10 of Cochlea 1, as an example. The values of their objective functions are shown in Table 9. The solution based on Croghan et al. (2023) improves the phased-array in terms of focusing, while it is surpassed by the median pattern and the optimum focusing solution. In terms of power consumption, inverse relations with respect to the focusing were observed. Fig. 28 shows the comparison in terms of current density distribution, where values of focusing F_c are clearly related to the narrowness of the shape of current density (the higher the focusing, the narrower the shape of the curve).

Simulations performed in this work were matched to the real data of transimpedance matrices of patients for the Nucleus CI512 implant, which were the ones available for this research at the Complejo Hospitalario Universitario Insular Materno Infantil de Gran Canaria.

Therefore the geometry of the FEM as described in Section 3.2 reproduces the distances of this implant type accordingly. Authors are aware that this device is not currently capable of producing the kind of multipolar stimulation that the present study has investigated, which depends mainly on the electronic capabilities of the implant. In any case, the methodology and procedure described in this work is applicable to any other implant and its associated geometry when clinical data were available. As future work, the application and analysis of multiobjective optimization of additional electrode designs (different electrode size, shape and/or spacing) and location (perimodiolar/lateral) are planned to be performed.

6. Conclusions

We have developed a computational model that combines FEM and evolutionary algorithms to simultaneously optimize focusing and power consumption in CI stimulation. For this goal, we have proposed two objective functions, one for focusing F_c and one for power consumption P.

Using a multiobjective optimization procedure, where high quality corner solutions were injected in the initial population, we obtained current profiles capable of improving the focusing and power consumption of both monopolar and phased-array stimulation, which are those used in practice. Specifically, Section 4.5 has handled the multiobjective optimization results, providing a set of equally optimum (from the mathematical point of view) designs, called non-dominated solutions. In our case, this set provides for each value of the power consumption the maximum associated possible focusing; or alternatively seen, for each value of the focusing, the minimum associated power consumption. It is the task of the expert or decision maker based on their preferences (in our case, the CI designer) to choose their preferable optimum design. We propose as interesting designs those starting with: (a) the design with equal focusing than the phased-array design but with lower power consumption; continuing with: (b) all designs that improve the phased-array stimulation in both objective functions (F_c and P); (c) the design with equal power consumption than phased-array but with increased focusing; and finally, (d) designs with higher power consumption than phased-array but better focusing, up to the design with best focusing. The final decision making choice depends on the CI manufacturer's policy supported by clinical evidence.

Additionally, an analysis of the best focusing solutions allowed to obtain design principles. The current pattern corresponding to maximum focusing shows alternating signs and decreasing values as we move away from the central active electrode. This allows the extraction of a pattern of currents built from the median values of the stimulating electrodes and common to all electrodes. It was even able to improve the focusing of the phased-array stimulation. The proposed median pattern requires a limited number of adjacent signals from the point of view of the central active electrode (+4/-4 in this study).

All the above could lead to common principles useful for the design of an improved multipolar stimulation of cochlear implants in practice.

As future work, in order to further improve the multi-objective optimization of this cochlear implant problem, it would be useful to propose customized operators. These could be based on the application of the innovization based methodology proposed in Ghosh, Deb, Goodman, and Averill (2022), where specific knowledge of the problem can be exploited, or other methodologies (e.g. Maskooki, Deb, and Kallio 2022).

CRediT authorship contribution statement

Marcos Hernández-Gil: Conceptualization, Software, Validation, Investigation, Writing – original draft, Writing – review & editing, Visualization. **Ángel Ramos-de-Miguel:** Conceptualization, Methodology, Formal analysis, Investigation, Writing - Review & Editing, Supervision. **David Greiner:** Conceptualization, Methodology, Software, Validation, Formal analysis, Investigation, Writing – original draft, Writing – review & editing, Visualization, Supervision. **Domingo Benítez:** Conceptualization, Methodology, Formal analysis, Investigation, Writing – review & editing. **Ángel Ramos-Macías:** Conceptualization, Methodology, Resources, Data curation, Writing – review & editing, Supervision. **José M. Escobar:** Conceptualization, Methodology, Software, Validation, Investigation, Resources, Writing – original draft, Writing – review & editing, Supervision, Project administration, Funding acquisition.

Declaration of competing interest

The authors declare that they have no known competing financial interests or personal relationships that could have appeared to influence the work reported in this paper.

Acknowledgments

Authors gratefully acknowledge the team of Miguel Ángel González Ballester from the Universitat Pompeu Fabra (Barcelona, Spain), for providing a three dimensional mesh of the cochlea based on the research in Mangado et al. (2018).

Funding

This research was partially supported by ACIISI Gobierno de Canarias and European FEDER Funds Grant EIS 2021 04. This work has been supported by: Ministerio de Ciencia, Innovación y Universidades, Gobierno de España, grant contract: PID2019-110185RB-C22; Agencia Canaria de Investigación, Innovación y Sociedad de la Información, Consejería de Economía, Conocimiento y Empleo del Gobierno de Canarias, grant contract: PROID 2020010022; and Consejería de Universidades, Ciencia e Innovación y Cultura del Gobierno de Canarias, grant contract: PRECOMP02 SD-24/03. The funders had no role in study design, data collection and analysis, decision to publish, or preparation of the manuscript.

Appendix. Total power supplied by the electrodes.

The expression (19) gives us the power dissipated in the electrolyte and the tissues associated with the resistive matrix $\mathbf{Z}_c$. This power has served as a starting point to develop an objective function that does not depend on the particular waveform of the input current i_{unit}. However, the total power supplied by the electrodes must also include the power dissipated in the double layer, associated with the matrix $\mathbf{D}(\omega)$. Thus, the total average power supplied by the electrodes is

$$P_{avg\backslash tot} = \frac{1}{T}\int_0^T \mathbf{i}^{\mathrm{T}}(t)\,\mathbf{v}(t)\,dt \tag{A.1}$$

where $\mathbf{v}(t) = \mathcal{F}^{-1}(\mathbf{Z}(\omega)\,\mathbf{I}(\omega))$, being $\mathbf{Z}(\omega) = \mathbf{D}(\omega) + \mathbf{Z}_c$ the transimpedance matrix. To evaluate this power, we will use the generalized Plancherel identity.

$$P_{avg\backslash tot} = \frac{1}{2\pi T}\int_{-\infty}^{\infty} \overline{\mathbf{I}^{\mathrm{T}}(\omega)}\mathbf{Z}(\omega)\,\mathbf{I}(\omega)\,d\omega = \boldsymbol{\alpha}^{\mathrm{T}}\left(\frac{1}{2\pi T}\int_{-\infty}^{\infty} |I_{unit}(\omega)|^2\mathbf{Z}(\omega)\,d\omega\right)\boldsymbol{\alpha} \tag{A.2}$$

In general, this integral cannot be calculated analytically, so it must be evaluated numerically. To calculate (A.2) we have to know the transimpedance matrix $\mathbf{Z}(\omega)$. The matrix $\mathbf{Z}_c$ is calculated through the conductive FEM model. Also, we know that the terms of the diagonal matrix $\mathbf{D}(\omega)$ are of the form $Z_{cpe} = K(\mathrm{j}\omega)^{-\beta}$. As discussed in Section 2, the specific values of K and β depend on the patient and the electrode considered. Taking into account the average values reported by Mesnildrey et al. (2020) for a total of 8 patients, we obtain an impedance $Z_{cpe} = 2.079\times10^6(\mathrm{j}\omega)^{-0.64}\Omega$. This is the impedance introduced in all the terms of the diagonal of $\mathbf{D}(\omega)$ in the next example.

Table A.10
Relative powers with respect to the PA stimulation including the effect of the double layer $\left(\frac{P_{avg}}{P_{avg,\mathrm{PA}}}\Big|_{tot}\right)$ and not including it $\left(\frac{P_{avg}}{P_{avg,\mathrm{PA}}}\right)$. Example for Cochlea 1 and electrode 10.

Power Ratios	MP	OF
$\frac{P_{avg}}{P_{avg,\mathrm{PA}}}\Big\|_{tot}$	0.159	3.275
$\frac{P_{avg}}{P_{avg,\mathrm{PA}}}$	0.273	3.002

As a test problem, let us consider the total powers delivered by the electrodes for monopolar stimulation, phased-array stimulation and optimum focusing taken the Cochlea 1 and the electrode 10. The input current $i_{unit}(t)$ is the pulse represented in Fig. 1, with an amplitude of 1 A, phase width of 25 μs and interphase gap width of 8 μs.

The relative powers $\frac{P_{avg\backslash tot}}{P_{avg}}$ for MP, PA and OF are $\frac{P_{avg\backslash tot}}{P_{avg}}\Big|_{\mathrm{MP}} = 1.477$, $\frac{P_{avg\backslash tot}}{P_{avg}}\Big|_{\mathrm{PA}} = 2.526$ and $\frac{P_{avg\backslash tot}}{P_{avg}}\Big|_{\mathrm{OF}} = 2.757$. Taking into account these ratios and the values of the objective function $P = \frac{P_{avg}}{P_{avg,\mathrm{PA}}}$ from Table 6 (electrode 10), we can calculate the MP and OF powers respect to the PA stimulation including the double layer. These results are shown in the Table A.10 compared with the values of the objective function $\frac{P_{avg}}{P_{avg,\mathrm{PA}}}$.

Table A.10 indicates that the power ratios exhibit little variation, regardless of whether the double layer is included or not. This suggests that the outcomes derived from an objective function that incorporates the double layer would not deviate significantly from those obtained with the function $P(\boldsymbol{\alpha})$ proposed in Section 3.4.2.

Data availability

Data will be made available on request.

References

Aebischer, P., Meyer, S., Caversaccio, M., & Wimmer, W. (2021). Intraoperative impedance-based estimation of cochlear implant electrode array insertion depth. *IEEE Transactions on Biomedical Engineering*, *68*(2), 545–555. http://dx.doi.org/10.1109/tbme.2020.3006934.

Ashida, G., & Nogueira, W. (2018). Spike-conducting integrate-and-fire model. *Eneuro*, *5*(4), ENEURO.0112–18.2018. URL http://dx.doi.org/10.1523/ENEURO.0112-18.2018.

Bouhlel, M. A., Hwang, J. T., Bartoli, N., Lafage, R., Morlier, J., & Martins, J. R. R. A. (2019). A python surrogate modeling framework with derivatives. *Advances in Engineering Software*, Article 102662. http://dx.doi.org/10.1016/j.advengsoft.2019.03.005.

Brockhoff, D., & Tušar, T. (2019). Benchmarking algorithms from the platypus framework on the biobjective bbob-biobj testbed. In *GECCO 2019*: *Vol. 3242*, *Proceedings of the Genetic and Evolutionary Computation Conference companion GECCO* (pp. 1905–1911). ACM, http://dx.doi.org/10.1145/3319619.3326896.

Cakmak, O., Pal, S., & Sahin, M. (2023). Improving the stimulation selectivity in the human cochlea by strategic selection of the current return electrode. *Frontiers in Audiology and Otology*, *1*, http://dx.doi.org/10.3389/fauot.2023.1259852.

Callejón-Leblic, M. A., Lazo-Maestre, M., Fratter, A., Ropero-Romero, F., Sánchez-Gómez, S., & Reina-Tosina, J. (2024). A full-head model to investigate intra and extracochlear electric fields in cochlear implant stimulation. *Physics in Medicine and Biology*, *69*(15), Article 155010. http://dx.doi.org/10.1088/1361-6560/ad5c38.

Cantrell, D. R., Inayat, S., Taflove, A., Ruoff, R. S., & Troy, J. B. (2007). Incorporation of the electrode–electrolyte interface into finite-element models of metal microelectrodes. *Journal of Neural Engineering*, *5*(1), 54. http://dx.doi.org/10.1088/1741-2560/5/1/006.

Carbonaro, D., Lucchetti, A., Audenino, A. L., Gries, T., Vaughan, T. J., & Chiastra, C. (2023). Multi-objective design optimization of bioresorbable braided stents. *Computer Methods and Programs in Biomedicine*, *242*, Article 107781. http://dx.doi.org/10.1016/j.cmpb.2023.107781.

Cassar, I. R., Titus, N. D., & Grill, W. M. (2017). An improved genetic algorithm for designing optimal temporal patterns of neural stimulation. *Journal of Neural Engineering*, *14*(6), Article 066013. http://dx.doi.org/10.1088/1741-2552/aa8270.

Coello, C., VanVeldhuizen, D., & Lamont, G. (2007). *Evolutionary algorithms for solving multi-objective problems*. Springer US, http://dx.doi.org/10.1007/978-0-387-36797-2.

Croghan, N., Krishnamoorthi, H., & Smith, Z. (2023). Multiple sound source encoding in hearing prostheses. (US2023082528A1), URL https://worldwide.espacenet.com/patent/search/family/070463566/publication/US2023082528A1?q=pn%3DUS2023082528A1.

de Nobel, J., Kononova, A. V., Briaire, J. J., Frijns, J. H., & Bäck, T. H. (2023). Optimizing stimulus energy for cochlear implants with a machine learning model of the auditory nerve. *Hearing Research*, *432*, Article 108741. http://dx.doi.org/10.1016/j.heares.2023.108741.

Deb, K. (2001). *Multi-objective optimization using evolutionary algorithms*. John Wiley and Sons, URL https://www.wiley.com/en-us/Multi+Objective+Optimization+using+Evolutionary+Algorithms-p-9780471873396.

Deb, K. (2023). An interview with kalyanmoy deb 2022 ACM fellow. *ACM SIGEVOlution*, *16*(1), 1–6. http://dx.doi.org/10.1145/3594261.3594262.

Deb, K., Bandaru, S., Greiner, D., Gaspar-Cunha, A., & Tutum, C. C. (2014). An integrated approach to automated innovization for discovering useful design principles: Case studies from engineering. *Applied Soft Computing*, *15*, 42–56. http://dx.doi.org/10.1016/j.asoc.2013.10.011.

Deb, K., Pratap, A., Agarwal, S., & Meyarivan, T. (2002). A fast and elitist multiobjective genetic algorithm: NSGA-II. *IEEE Transactions on Evolutionary Computation*, *6*(2), 182–197. http://dx.doi.org/10.1109/4235.996017.

Ding, S., Yan, L., Sun, Y., Ren, Y., Zhou, X., & Fu, Q. (2024). Evolutionary multi-objective optimization for high-speed railway train timetable rescheduling with optimal/suboptimal solutions into initial population. In *2024 Australian and New Zealand Control Conference* (pp. 259–264). IEEE, http://dx.doi.org/10.1109/anzcc59813.2024.10432899.

Dokos, S. (2017). *Lecture Notes in Bioengineering*, *Modelling organs, tissues, cells and devices*. Springer Berlin Heidelberg, http://dx.doi.org/10.1007/978-3-642-54801-7.

Emmerich, M. T. M., & Deutz, A. H. (2018). A tutorial on multiobjective optimization: fundamentals and evolutionary methods. *Natural Computing*, *17*(3), 585–609. http://dx.doi.org/10.1007/s11047-018-9685-y.

Essaid, B., Kheddar, H., Batel, N., Chowdhury, M. E. H., & Lakas, A. (2024). Artificial intelligence for cochlear implants: Review of strategies, challenges, and perspectives. *IEEE Access*, *12*, 119015–119038. http://dx.doi.org/10.1109/access.2024.3429524.

Franks, W., Schenker, I., Schmutz, P., & Hierlemann, A. (2005). Impedance characterization and modeling of electrodes for biomedical applications. *IEEE Transactions on Biomedical Engineering*, *52*(7), 1295–1302. http://dx.doi.org/10.1109/tbme.2005.847523.

Frijns, J. H., Dekker, D. M., & Briaire, J. J. (2011). Neural excitation patterns induced by phased-array stimulation in the implanted human cochlea. *Acta Oto-Laryngologica*, *131*(4), 362–370. http://dx.doi.org/10.3109/00016489.2010.541939.

Garcia, S., & Herrera, F. (2008). An extension on 'Statistical Comparisons of Classifiers over Multiple Data Sets" for all pairwise comparisons. *Journal of Machine Learning Research*, *9*, 2677–2694.

Ghosh, A., Deb, K., Goodman, E., & Averill, R. (2022). A user-guided innovization-based evolutionary algorithm framework for practical multi-objective optimization problems. *Engineering Optimization*, *55*(12), 2084–2096. http://dx.doi.org/10.1080/0305215x.2022.2144275.

Gong, C., Nan, Y., Pang, L. M., Zhang, Q., & Ishibuchi, H. (2023). Effects of including optimal solutions into initial population on evolutionary multiobjective optimization. In *Proceedings of the Genetic and Evolutionary Computation Conference* (pp. 661–669). ACM, http://dx.doi.org/10.1145/3583131.3590515.

Greiner, D., Emperador, J. M., & Winter, G. (2004). Single and multiobjective frame optimization by evolutionary algorithms and the auto-adaptive rebirth operator. *Computer Methods in Applied Mechanics and Engineering*, *193*(33–35), 3711–3743. http://dx.doi.org/10.1016/j.cma.2004.02.001.

Greiner, D., Gaspar-Cunha, A., Hernandez-Sosa, D., Minisci, E., & Zamuda, A. (2022). *Evolutionary algorithms in engineering design optimization*. MDPI, http://dx.doi.org/10.3390/books978-3-0365-2715-4.

Greiner, D., Periaux, J., Emperador, J. M., Galván, B., & Winter, G. (2017). Game theory based evolutionary algorithms: A review with Nash applications in structural engineering optimization problems. *Archives of Computational Methods in Engineering*, *24*(4), 703–750. http://dx.doi.org/10.1007/s11831-016-9187-y.

Greiner, D., Periaux, J., Quagliarella, D., Magalhaes-Mendes, J., & Galván, B. (2018). Evolutionary algorithms and metaheuristics: Applications in engineering design and optimization. *Mathematical Problems in Engineering*, *2018*, 1–4. http://dx.doi.org/10.1155/2018/2793762.

Hadka, D. (2024). Platypus: A framework for evolutionary computing in Python (version 1.4.1) [computer software]. URL https://github.com/Project-Platypus/Platypus.

Hanekom, T., & Hanekom, J. J. (2016). Three-dimensional models of cochlear implants: A review of their development and how they could support management and maintenance of cochlear implant performance. *Network: Computation in Neural Systems*, *27*(2–3), 67–106. http://dx.doi.org/10.3109/0954898x.2016.1171411.

Henkin, Y., Kaplan-Neeman, R., Muchnik, C., Kronenberg, J., & Hildesheimer, M. (2003). Changes over time in electrical stimulation levels and electrode impedance values in children using the Nucleus 24M cochlear implant. *International Journal of Pediatric Otorhinolaryngology*, *67*(8), 873–880. http://dx.doi.org/10.1016/s0165-5876(03)00131-9.

Hodgkin, A. L., & Huxley, A. F. (1952). A quantitative description of membrane current and its application to conduction and excitation in nerve. *The Journal of Physiology*, *117*(4), 500–544. http://dx.doi.org/10.1113/jphysiol.1952.sp004764.

Hussain, M. A., Grill, W. M., & Pelot, N. A. (2024). Highly efficient modeling and optimization of neural fiber responses to electrical stimulation. *Nature Communications*, *15*(1), http://dx.doi.org/10.1038/s41467-024-51709-8.

Jolly, C., Spelman, F., & Clopton, B. (1996). Quadrupolar stimulation for cochlear prostheses: modeling and experimental data. *IEEE Transactions on Biomedical Engineering*, *43*(8), 857–865. http://dx.doi.org/10.1109/10.508549.

Joucla, S., Branchereau, P., Cattaert, D., & Yvert, B. (2012). Extracellular neural microstimulation may activate Much Larger Regions than expected by simulations: A combined experimental and modeling study. In E. Vasilaki (Ed.), *PLoS ONE*, *7*(8), Article e41324. http://dx.doi.org/10.1371/journal.pone.0041324.

Kalkman, R. K., Briaire, J. J., & Frijns, J. H. (2015). Current focussing in cochlear implants: An analysis of neural recruitment in a computational model. *Hearing Research*, *322*, 89–98. http://dx.doi.org/10.1016/j.heares.2014.12.004.

Kjer, H. M., Fagertun, J., Wimmer, W., Gerber, N., Vera, S., Barazzetti, L., Mangado, N., Ceresa, M., Piella, G., Stark, T., Stauber, M., Reyes, M., Weber, S., Caversaccio, M., Gonzalez Ballester, M. A., & Paulsen, R. R. (2018). Patient-specific estimation of detailed cochlear shape from clinical CT images. *International Journal of Computer Assisted Radiology and Surgery*, *13*(3), 389–396. http://dx.doi.org/10.1007/s11548-017-1701-7.

Liu, Z. (2023). *Patient-specific modeling of cochlear implants* (Ph.D. thesis), Vanderbilt University Graduate School, URL https://ir.vanderbilt.edu/items/b81ba8b3-de48-4c0e-900a-f21e1bd4247c.

Mahnam, A., Hashemi, S. M. R., & Grill, W. M. (2008). Computational evaluation of methods for measuring the spatial extent of neural activation. *Journal of Neuroscience Methods*, *173*(1), 153–164. http://dx.doi.org/10.1016/j.jneumeth.2008.05.019.

Malherbe, T. K., Hanekom, T., & Hanekom, J. J. (2015a). Constructing a three-dimensional electrical model of a living cochlear implant user's cochlea. *International Journal for Numerical Methods in Biomedical Engineering*, *32*(7), Article e02751. http://dx.doi.org/10.1002/cnm.2751.

Malherbe, T., Hanekom, T., & Hanekom, J. (2015b). The effect of the resistive properties of bone on neural excitation and electric fields in cochlear implant models. *Hearing Research*, *327*, 126–135. http://dx.doi.org/10.1016/j.heares.2015.06.003.

Mangado, N., Ceresa, M., Duchateau, N., Kjer, H. M., Vera, S., Dejea Velardo, H., Mistrik, P., Paulsen, R. R., Fagertun, J., Noailly, J., Piella, G., & González Ballester, M. Á. (2015). Automatic model generation framework for computational simulation of cochlear implantation. *Annals of Biomedical Engineering*, *44*(8), 2453–2463. http://dx.doi.org/10.1007/s10439-015-1541-y.

Mangado, N., Pons-Prats, J., Coma, M., Mistrík, P., Piella, G., Ceresa, M., & Ballester, M. Á. G. (2018). Computational evaluation of cochlear implant surgery outcomes accounting for uncertainty and parameter variability. *Frontiers in Physiology*, *9*, http://dx.doi.org/10.3389/fphys.2018.00498.

Maskooki, A., Deb, K., & Kallio, M. (2022). A customized genetic algorithm for bi-objective routing in a dynamic network. *European Journal of Operational Research*, *297*(2), 615–629. http://dx.doi.org/10.1016/j.ejor.2021.05.018.

McAdams, E. T., & Jossinet, J. (1992). A physical interpretation of Schwan's limit current of linearity. *Annals of Biomedical Engineering*, *20*(3), 307–319. http://dx.doi.org/10.1007/bf02368533.

Mesnildrey, Q., Macherey, O., Herzog, P., & Venail, F. (2019). Impedance measures for a better understanding of the electrical stimulation of the inner ear. *Journal of Neural Engineering*, *16*, Article 016023. http://dx.doi.org/10.1088/1741-2552/aaecff.

Mesnildrey, Q., Venail, F., Carlyon, R. P., & Macherey, O. (2020). Polarity sensitivity as a potential correlate of neural degeneration in cochlear implant users. *Journal of the Association for Research in Otolaryngology*, *21*(1), 89–104. http://dx.doi.org/10.1007/s10162-020-00742-7.

de Miguel, Á. R., Escobar, J. M., Greiner, D., Benítez, D., Rodríguez, E., Oliver, A., Hernández, M., & Ramos-Macías, Á. (2022). A phenomenological computational model of the evoked action potential fitted to human cochlear implant responses. In W. Nogueira (Ed.), *PLOS Computational Biology*, *18*(5), Article e1010134. http://dx.doi.org/10.1371/journal.pcbi.1010134.

de Miguel, Á. R., Escobar, J. M., Greiner, D., & Ramos-Macías, Á. (2018). A multiobjective optimization procedure for the electrode design of cochlear implants. *International Journal for Numerical Methods in Biomedical Engineering*, *34*(8), Article e2992. http://dx.doi.org/10.1002/cnm.2992.

Nogueira, W., Schurzig, D., Büchner, A., Penninger, R. T., & Würfel, W. (2016). Validation of a cochlear implant patient-specific model of the voltage distribution in a clinical setting. *Frontiers in Bioengineering and Biotechnology*, *4*, http://dx.doi.org/10.3389/fbioe.2016.00084.

Nowak, L. G., & Bullier, J. (1996). Spread of stimulating current in the cortical grey matter of rat visual cortex studied on a new in vitro slice preparation. *Journal of Neuroscience Methods*, *67*(2), 237–248. http://dx.doi.org/10.1016/0165-0270(96)00065-9.

Osaba, E., Villar-Rodriguez, E., Ser, J. D., Nebro, A. J., Molina, D., LaTorre, A., Suganthan, P. N., Coello, C. A. C., & Herrera, F. (2021). A Tutorial On the design, experimentation and application of metaheuristic algorithms to real-World optimization problems. *Swarm and Evolutionary Computation*, *64*, Article 100888. http://dx.doi.org/10.1016/j.swevo.2021.100888.

Potrusil, T., Heshmat, A., Sajedi, S., Wenger, C., Chacko, L. J., Glueckert, R., Schrott-Fischer, A., & Rattay, F. (2020). Finite element analysis and three-dimensional reconstruction of tonotopically aligned human auditory fiber pathways: A computational environment for modeling electrical stimulation by a cochlear implant based on micro-CT. *Hearing Research*, *393*, Article 108001. http://dx.doi.org/10.1016/j.heares.2020.108001.

Price, K. V. (2013). Differential evolution. In *Handbook of optimization* (pp. 187–214). Springer Berlin Heidelberg, http://dx.doi.org/10.1007/978-3-642-30504-7_8.

Randy K. Kalkman, J. J. B., & Frijns, J. H. M. (2016). Stimulation strategies and electrode design in computational models of the electrically stimulated cochlea: An overview of existing literature. *Network: Computation in Neural Systems*, *27*(2–3), 107–134. http://dx.doi.org/10.3109/0954898X.2016.1171412.

Richardot, A., & McAdams, E. (2002). Harmonic analysis of low-frequency bioelectrode behavior. *IEEE Transactions on Medical Imaging*, *21*(6), 604–612. http://dx.doi.org/10.1109/tmi.2002.800576.

Ruan, X., Li, K., Derbel, B., & Liefooghe, A. (2020). Surrogate assisted evolutionary algorithm for medium scale multi-objective optimisation problems. In *Proceedings of the 2020 Genetic and Evolutionary Computation Conference* (pp. 560–568). ACM, http://dx.doi.org/10.1145/3377930.3390191.

Saba, R. (2012). *Cochlear implant modelling: stimulation and power consumption* (Ph.D. thesis), University of Southampton, URL https://eprints.soton.ac.uk/348818/.

Saba, R., Elliott, S. J., & Wang, S. (2014). Modelling the effects of cochlear implant current focusing. *Cochlear Implants International*, *15*(6), 318–326. http://dx.doi.org/10.1179/1754762814Y.0000000081.

Smith, Z. M., Parkinson, W. S., & Long, C. J. (2013). Multipolar current focusing increases spectral resolution in cochlear implants. In *2013 35th Annual International Conference of the IEEE Engineering in Medicine and Biology Society* (pp. 2796–2799). IEEE, http://dx.doi.org/10.1109/embc.2013.6610121.

Tehovnik, E. J., Tolias, A. S., Sultan, F., Slocum, W. M., & Logothetis, N. K. (2006). Direct and indirect activation of cortical neurons by electrical microstimulation. *Journal of Neurophysiology*, *96*(2), 512–521. http://dx.doi.org/10.1152/jn.00126.2006.

Toledo, R., Aznárez, J., Greiner, D., & Maeso, O. (2017). A methodology for the multi-objective shape optimization of thin noise barriers. *Applied Mathematical Modelling*, *50*, 656–675. http://dx.doi.org/10.1016/j.apm.2017.06.020.

van den Honert, C., & Kelsall, D. C. (2007). Focused intracochlear electric stimulation with phased array channels. *Journal of the Acoustical Society of America*, *121*(6), 3703–3716. http://dx.doi.org/10.1121/1.2722047.

Vellinga, D., Bruijn, S., Briaire, J. J., Kalkman, R. K., & Frijns, J. H. M. (2017). Reducing interaction in simultaneous paired stimulation with CI. In F.-G. Zeng (Ed.), *PLOS ONE*, *12*(2), Article e0171071. http://dx.doi.org/10.1371/journal.pone.0171071.

Viana, F. A. C. (2015). A tutorial on latin hypercube design of experiments. *Quality and Reliability Engineering International*, *32*(5), 1975–1985. http://dx.doi.org/10.1002/qre.1924.

Virtanen, P., Gommers, R., Oliphant, T. E., et al. (2020). SciPy 1.0: fundamental algorithms for scientific computing in Python. *Nature Methods*, *17*(3), 261–272. http://dx.doi.org/10.1038/s41592-019-0686-2.

Wongsarnpigoon, A., & Grill, W. M. (2010). Energy-efficient waveform shapes for neural stimulation revealed with a genetic algorithm. *Journal of Neural Engineering*, *7*(4), Article 046009. http://dx.doi.org/10.1088/1741-2560/7/4/046009.

Wu, C.-C., & Luo, X. (2016). Excitation patterns of standard and steered partial tripolar stimuli in cochlear implants. *Journal of the Association for Research in Otolaryngology*, *17*(2), 145–158. http://dx.doi.org/10.1007/s10162-015-0549-1.

Xu, Y., Luo, C., & You, Z. (2018). Optimization of cochlear implant stimulation resolution using an intracochlear electric potential model. *Computers in Biology and Medicine*, *94*, 99–105. http://dx.doi.org/10.1016/j.compbiomed.2017.12.016.

Zhang, G., Chen, R., Ghorbani, H., Li, W., Minasyan, A., Huang, Y., Lin, S., & Shao, M. (2025). Artificial intelligence-enabled innovations in cochlear implant technology: Advancing auditory prosthetics for hearing restoration. *Bioengineering & Translational Medicine*, http://dx.doi.org/10.1002/btm2.10752.

Zhu, C., Byrd, R. H., Lu, P., & Nocedal, J. (1997). Algorithm 778: L-BFGS-B: Fortran subroutines for large-scale bound-constrained optimization. *Association for Computing Machinery. Transactions on Mathematical Software*, *23*(4), 550–560. http://dx.doi.org/10.1145/279232.279236.

Zhu, Z., Tang, Q., Zeng, F.-G., Guan, T., & Ye, D. (2012). Cochlear-implant spatial selectivity with monopolar, bipolar and tripolar stimulation. *Hearing Research*, *283*(1–2), 45–58. http://dx.doi.org/10.1016/j.heares.2011.11.005.

Zitzler, E., Thiele, L., Laumanns, M., Fonseca, C., & da Fonseca, V. (2003). Performance assessment of multiobjective optimizers: an analysis and review. *IEEE Transactions on Evolutionary Computation*, *7*(2), 117–132. http://dx.doi.org/10.1109/tevc.2003.810758.